Master's thesis

NTNU
Norwegian University of Science and Technology
Faculty of Engineering
Department of Marine Technology

Andreas Bohinen Kvernmo

Ship collisions with floating offshore wind turbine

Master's thesis in Marine Technology
Supervisor: Jørgen Amdahl
Co-supervisor: Zhaolong Yu
June 2023

NTNU
Norwegian University of
Science and Technology

Andreas Bohinen Kvernmo

Ship collisions with floating offshore wind turbine

Master's thesis in Marine Technology
Supervisor: Jørgen Amdahl
Co-supervisor: Zhaolong Yu
June 2023

Norwegian University of Science and Technology
Faculty of Engineering
Department of Marine Technology

NTNU
Norwegian University of
Science and Technology

NTNU
Norges teknisk-naturvitenskapelige universitet
Institutt for marin teknikk

MASTER THESIS 2023

for

Stud. **Andreas Bohinen Kvernmo**

Ship collisions with floating offshore wind turbine

Skipkollisjoner med flytende offshore vindtrubiner

Background

Wind power is considered "green" energy and a large number of wind turbines have been erected on land. However, the wind energy potential is considerably larger in open seas; the environmental impact is smaller, and consequently an increasing part of the new wind farms are installed offshore.
Wind farms will be serviced by vessels and thus the risk of impacts exists. In addition, many offshore wind farms will be located close to ship traffic lanes and thus the risk of collision with merchant vessel or even large tankers become of concern. For floating and bottom supported wind turbines several failure modes are possible, among others:

- The tower may collapse and fall onto - or away from the ship. Failure may possibly be influence by local buckling. If the tower collapses towards the ship, the ship may be hit by the nacelle.
- The acceleration of the nacelle may exceed acceptable levels
- The rotor blades may be subjected to significant out-of-plane vibrations so that they hit the tower
- The foundation, e.g. monopiles or tether for TLPs, may fail
- Penetration of empty compartments may cause capsizing of floating installations

Assessment structural resistance has typically been placed on accidental events as those described above with a low probability of occurrence. Recently focus has also been placed on more frequent events, with an annual probability of occurrence in the range of 0.01-0.1. Such impacts will have to be considered in the Ultimate Limit State (ULS) as opposed to the above events that have to be checked in the Accidental Limit State (ALS).
Normally, ULS checks assume the structure to behave elastically. This can be difficult to achieved with ship collisions, as small damages in the form of dents are likely. This should,

however, not be considered critical, if the structure with dents can comply with the ULS criteria otherwise.

The objective of this investigation is to investigate the damage caused by ULS ship impacts and to determine the acceptable damage level in view of the residual strength of the structure.

Scope of work

The following topics should be addressed:

1. Brief description of the selected floating offshore wind turbine structure(s) for ship impact assessment. Describe relevant collision scenarios (w.r.t. to ship size, contact locations, speed, impact angle etc.). Collisions with both turbine tower/column, braces or joints with various configurations should be considered.

2. Prepare a detailed local model for ship collision analysis with LS_DYNA. Various components may be studied, such as the turbine tower , The wind turbine requires a detailed shell finite element model in the contact area, large enough to avoid violation of boundary conditions. If possible, perform a mesh size convergence study LS-DYNA. Available ship models of bow structure, side shell or stern structure will be provided. If necessary local ship models should be connected to a beam model representing the global ship motions.

3. Conduct simulations for various degrees of indentation, representing small and moderate impacts. Check the energy audit in the collision and clarify whether the hourglass energy is acceptably small. Describe and discuss the damage and energy dissipation in the platform component.

4. Conduct residual strength analysis of the structure with selected damage. For the tower the local model should be subjected to an increasing bending moment . For other components it could be by combined bending and axial force.

5. Propose analytic models for assessment of the denting resistance of tubular members/circular shells and residual strength assessment of damaged tubulars. Discuss application of partial safety factors that shall be applied in the ULS design against impacts; shall it be on kinetic energy or on loads?

6. Conclusions and recommendations for further work

Literature studies of specific topics relevant to the thesis work may be included.

The work scope may prove to be larger than initially anticipated. Subject to approval from the supervisor, topics may be deleted from the list above or reduced in extent.

In the thesis the candidate shall present his personal contribution to the resolution of problems within the scope of the thesis work.

Theories and conclusions should be based on mathematical derivations and/or logic reasoning identifying the various steps in the deduction.

The candidate should utilize the existing possibilities for obtaining relevant literature.

The thesis should be organized in a rational manner to give a clear exposition of results, assessments, and conclusions. The text should be brief and to the point, with a clear language. Telegraphic language should be avoided.

The thesis shall contain the following elements: A text defining the scope, preface, list of contents, summary, main body of thesis, conclusions with recommendations for further work, list of symbols and acronyms, references and (optional) appendices. All figures, tables and equations shall be numerated.

The supervisor may require that the candidate, in an early stage of the work, presents a written plan for the completion of the work. The plan should include a budget for the use of computer and laboratory resources which will be charged to the department. Overruns shall be reported to the supervisor.

The original contribution of the candidate and material taken from other sources shall be clearly defined. Work from other sources shall be properly referenced using an acknowledged referencing system.

The report shall be submitted in two copies:
- Signed by the candidate
- The text defining the scope included
- In bound volume(s)
- Drawings and/or computer prints which cannot be bound should be organised in a separate folder.

Supervisor:
Prof. Jørgen Amdahl
Ass. professor Zhaolong Yu

Deadline: June 11, 2023

Trondheim, January 15 2023

Jørgen Amdahl

Abstract

Offshore wind is a renewable energy source that is receiving a lot of focus and attention. Among the benefits of offshore wind energy is improved wind conditions that, along with the possibility of increasing the size of the turbines, give a larger energy potential than onshore wind. Moreover, introducing floating substructures means less sensitivity to water depth and seabed conditions and less strict space constraints. This may, however, lead to higher needs for maintenance and service visits to the turbines. The vessels may need an increase in size, and the conditions may be harsher. The consequences of collisions can range from minor structural damages to the collapse of the turbine, which in turn could endanger the vessel crew, should the tower collapse towards or onto the vessel deck.

Therefore, classification societies such as DNV and Bureau Veritas have created standards for the design of offshore turbines to ensure that the risk of catastrophic consequences is limited. These standards include rules and regulations regarding design against both accidental and functional impact loads. These standards, in addition to the theory behind collision mechanics, regarding the dissipation of energy, the force-deformation relationship, and buckling theory, have been investigated.

To evaluate proposed analytical models for the assessment of both denting resistance of tubular members and the residual strength of damaged tubulars, the non-linear finite element software LS-DYNA has been used to simulate collisions. Models of both the tower and several parts of a modern supply vessel have been used in order to simulate and evaluate the damage and energy dissipation in the collision.

Firstly, a mesh convergence study is performed to evaluate the inaccuracies that can arise with different mesh sizes. The results show little deviation for the chosen mesh sizes. Secondly, collision simulations between the tower section and the bulb, forecastle, side, and stern corner are performed to evaluate the impact forces and the deformation of the structures. The results show that for the vessel, the force-deformation relationship agrees quite well with what is expected from proposed analytical models. As for the tower, there is more deviance from the expected results, as they are generally too conservative and underestimate the resistance in the tower. Finally, residual strength analyses are performed in order to evaluate the effects of indentation on the bending moment capacity. The results again differ from proposed analytical models. However, in this case, the models are not conservative enough in comparison to the results obtained in this thesis, and the

effects of indentations are far bigger than anticipated. They show that only small indentations will seriously affect the towers ability to comply with ULS criteria.

Sammendrag

Offshore vind er en fornybar energikilde som får mye fokus. Blant fordelene med offshore vind-energi er for eksempel bedre vind-forhold og større muligheter til å øke turbinstørrelsen sammenlignet med landbaserte turbiner. I tillegg, om man bruker flytende konstruksjoner, vil turbinene kunne plasseres steder hvor man ikke trenger å ta hensyn til havdybde og plassrestriksjoner i like stor grad. Dette kan riktignok føre til større behov for vedlikehold og reparasjonsbesøk til turbinene. Disse vedlikeholdsfartøyene kan måtte økes i størrelse og forholdene rundt turbinene kan være tøffere. Konsekvensen av kollisjoner kan variere fra små skader på konstruksjonen, til at turbinen kollapser, noe som kan ha fatale konsekvenser om tårnet faller mot fartøy og mannskap.

Derfor har klasseselskap som DNV og Bureau Veritas fastsatt standarder for design av offshore vindturbiner, for å minimere risikoen ved kollisjoner. Disse standardene inneholder regler og restriksjoner om design mot både uventede of mer forventede ulykker. Disse reguleringene, i tillegg til teori angående energiopptak, kraft-deformasjons forholdet, og knekning har blitt studert.

For å vurdere ulike metoder for å anslå resistansen mot bulking av sylindere samt reststyrke i allerede skadde sylindere, har programmet LS-DYNA blitt brukt for å simulere kollisjoner. Modeller for både tårnet og de ulike delene av skipet har blitt brukt til simuleringene.

Først ble det utført en mesh konvergens-studie for å bestemme forskjeller som kan oppstå ved forskjellige mesh-størrelser. Studien viste at det var små forskjeller for det relevante resultatområdet for de valgte størrelsene. Så ble kollisjonssimuleringer kjørt for både bulb, bakk, side og akterhjørnet for å beregne kraft-deformasjonskurver. For skipet stemmer resultatene ganske godt overens med de allerede anbefalte kurvene. For tårnet er det større forskjeller. Der er de anbefalte metodene ofte konservative og undervurderer tårnets resistanse mot bulking. Til slutt ble en reststyrke-analyse gjort, for å vurdere effekten bulker har på tårnets evne til å etterkomme kravene til styrke. Igjen er det forskjeller på resultatene og anbefalte metoder. I dette tilfellet er ikke metodene konservative nok, og i følge resultatene i denne analysen vil bulker i tårnet senke reststyrken betydelig mer enn forventet. De tilsier at bare små bulker er nok til at tårnet ikke etterkommer styrkekriteriene.

Preface

This Master's thesis is the final part of the Master of Science degree in Marine Technology at the Norwegian University of Science and Technology (NTNU) with a specialization in Marine Structures. The thesis continues the work done in the project thesis in the fall of 2022 and is done in the spring of 2023 and serves as a culmination of the five-year study program.

The problem description was proposed by supervisor Professor Jørgen Amdahl, and the topic is ship collision with floating offshore wind turbines. The objective is to assess the resistance and residual strength of a turbine subjected to ULS ship impacts. The work has been challenging but provided a better understanding of the consequences, theory, and regulations regarding both offshore wind turbines in general, and also the impact between turbines and vessels. As a lot of relevant literature and other sources had been collected during the project thesis work, the majority of the time spent and challenges faced came from learning and using the LS-DYNA software. However, the entire process has been more efficient by using the supercomputer Fram in the simulations.

I would like to thank my supervisor Professor Jørgen Amdahl for weekly guidance meetings that were crucial for the progress during the spring. Also, I would like to thank co-supervisor Associate Professor Zhaolong Yu, especially for helping with the LS-DYNA software and the simulation models, in addition to accessing the Fram supercomputer. Also, he was available for guidance when Professor Amdahl was on leave. Finally, I would like to thank Ph.D. Candidate Stina Bjørgo Fimreite for additional guidance in performing residual strength analysis in LS-DYNA.

Andreas Bohinen Kvernmo
Trondheim, 10.06.2023

Nomenclature

$\dot{\eta}$	Relative velocity in η direction
$\dot{\xi}$	Relative velocity in ξ direction
η	η direction in local coordinate system
μ	Ratio between impulses in η and ξ direction
μ_c	Critical ratio between impulses in η and ξ direction
ψ	Buckling coefficient for plane plate
ρ	knock-down factor
σ_{cl}	Classical elastic buckling resistance
σ_{cr}	Critical stress
ξ	ξ direction in local coordinate system
a_i	Installation added mass
a_s	Ship added mass
B	Width of contact area
C	Buckling coefficient
CoG	Center of Gravity
DOF	Degree Of Freedom
E_η	Lost Kinetic Energy in η direction

E_ξ	Lost Kinetic Energy in ξ direction
E_s, i	Installation dissipated energy
E_s, s	Ship dissipated energy
E_s	Strain energy
F_η	Impact force in η direction
F_ξ	Impact force in ξ direction
FE	Finite Element
LKE	Lost Kinetic Energy
m_i	Installation mass
m_s	Ship mass
N_{Rd}	Design axial compressive resistance
N_{sd}	Design axial compressive force
T	Time
v_i	Installation velocity
v_s	Impact speed
w_d	Dent depth
Z	Batdorf Parameter
DP	Dynamic Positioning

Table of Contents

List of Figures

List of Tables

Chapter 1

Introduction

In the fight against climate change, several organizations are working on ways to reduce greenhouse gases and find new renewable energy sources. At the Glasgow Climate Conference over 200 countries signed a pact to keep the goal of limiting the global temperatures from rising more than 1.5 °C alive (UN 2021). This requires actions across sectors, including increasing the renewable energy share to 32% (Commission 2019). The European Commission believes that offshore wind represents a significant opportunity (Commission 2022), and, according to the International Energy Agency, the offshore wind market had a growth of almost 30% per year between 2010 and 2018, due to rapidly maturing technology (IEA 2019).

As this is one of the renewable technologies with the best potential for up-scaling, the EU targets to increase the installed capacity from 12 GW in 2020 to at least 60 GW in 2030 and 300 GW by 2050 (Commission 2020). Offshore wind offers a higher energy potential due to higher quality of wind sources, with stronger winds and less turbulence. Additionally, there is less sight and sound pollution (Ren et al. 2022).

Currently, floating wind farm concepts are receiving a lot of attention (Ren et al. 2022). Floating wind farms are less sensitive to water depth and seabed conditions, compared to bottom-fixed structures. This allows for the installation of several turbines without the same constraints regarding space and planning, with the sites having a higher wind energy potential (Tong 1998).

The service and supply vessels operating on and around the turbines may accidentally collide with the turbines. In addition, wind farms may be located close

to areas with high ship traffic density, which means that there is also a possibility of collision between larger merchant vessels and turbines (Yu, Amdahl et al. 2022). To date, research regarding collisions between ships and wind farms is mainly limited to impacts between vessels and bottom-fixed structures. This is because bottom-fixed wind farms have been operational for years, while currently there are few commercial FOWTs. To capture more clean energy, the number of FOWTs is going to increase, and therefore investigating impacts between vessels and floating structures is relevant (Ren et al. 2022).

1.1 Objective and approach

The main objective of this Master's thesis is to assess the damage caused by ULS ship impacts with floating offshore wind turbines and to then determine the acceptable damage level regarding the residual strength of the structure. This is done by performing nonlinear collision and residual strength analyses in the FEM software LS-DYNA and comparing them to relevant analytical models and criteria. The full scope of work is presented at the start of the thesis.

This objective is met by first gathering and studying relevant literature and reports, including information on offshore wind energy, relevant regulations and practices, and theoretical knowledge on the mechanics of ship collisions. Some of this was done during the fall of 2022 for the project thesis, while some is done during the early phase of this Master's thesis. The second part of the process was modeling and performing collision simulations and residual strength assessments in LS-DYNA. This represented the majority of time and effort during the spring of 2023. The final part of the process includes presenting and discussing the results and the comparison to established models.

The thesis is divided into 10 chapters following this introduction.

- **Chapter 2** - Background study regarding floating offshore wind turbines including statistics and descriptions of relevant wind turbines and wind farms.
- **Chapter 3** - Descriptions of relevant collision scenarios, including both causes and consequences of the collisions, in addition to relevant reported accidents.
- **Chapter 4** - Investigation of rules and regulations regarding the design of offshore wind turbines, in addition to relevant theory and analytical models

for assessing denting resistance and residual strength.

- **Chapter 5** - Description of the FEM software LS-DYNA.
- **Chapter 6** - Description of the collision modeling in LS-DYNA, with relevant information about the vessel and tower models.
- **Chapter 7** - The mesh convergence study performed is described, and the results of this are presented.
- **Chapter 8** - Results from the collision analyses between the tower and vessel models for the bulb, forecastle, shipside, and stern corner collisions.
- **Chapter 9** - The residual strength analyses are performed and presented.
- **Chapter 10** - Discussion and conclusion.
- **Chapter 11** - Recommendations for further work.

In agreement with the supervisors, it was deemed sufficient to assess only collisions with and residual strength of the tower, as opposed to for example columns, braces, and joints as formulated in the assignment. In addition, it was deemed not necessary to connect a beam model to the local ship models. Also, the application of partial safety factors is discussed, however, there is very little relevant literature on it. Finally, the decision in agreement with the supervisor was to evaluate existing analytical models for assessment of resistance to indentation in tubular members and residual strength of damaged tubulars, rather than propose new models.

Chapter 2

Background

The first offshore wind farm was commissioned in Denmark in 1991, and since then, increased focus on renewable energy has resulted in a rise in offshore wind farms (Ørsted 2019). Currently, Europe is the world leader in offshore wind power, but the trend is growing globally, including in the US which aims for 30 GW by 2030 (WindEurope 2022). Figure 2.1 shows the mean wind power density across the north sea and the Atlantic Ocean up to at least 200 km offshore. Higher wind power density indicates better wind resources (Energydata.info 2023). The figure shows that there are good opportunities to exploit wind resources, especially off the coast of northern Europe and North America.

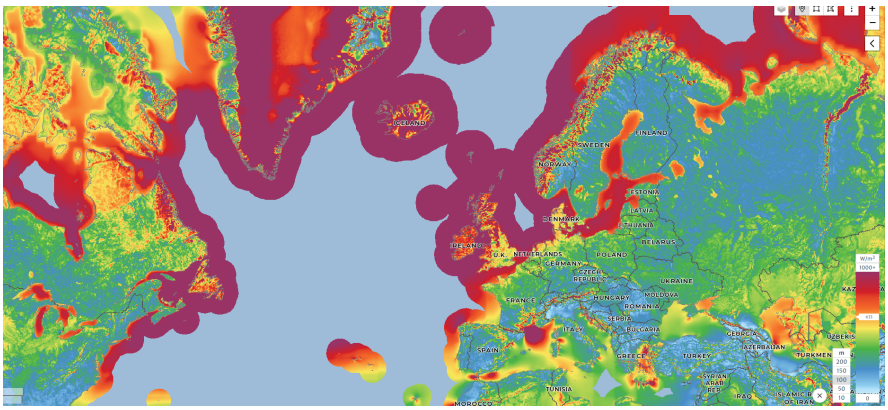

Figure 2.1: Mean wind power density at 100 m above sea level (Energydata.info 2023).

2.1 Key trends and statistics

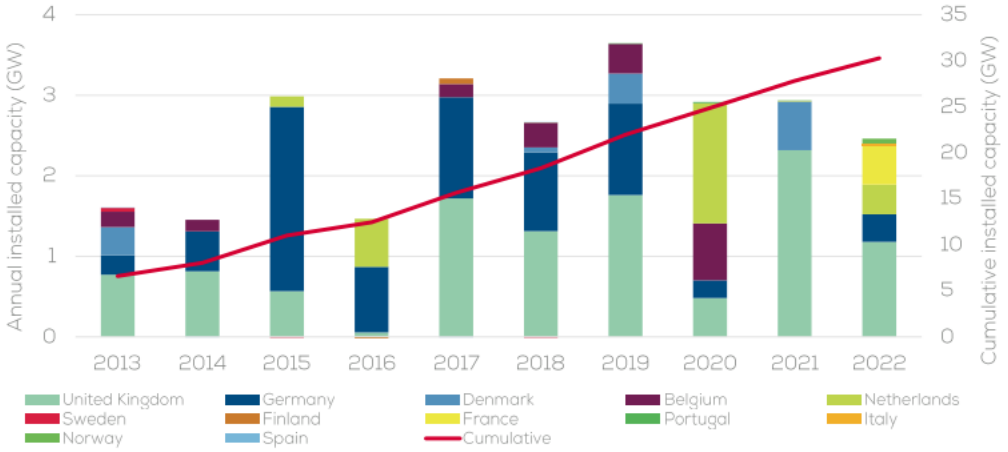

Figure 2.2: Annual and cumulative installed offshore wind power capacity in Europe (WindEurope 2023).

Figure 2.2 shows the annual and cumulative installed capacity for offshore wind energy in Europe. It shows a steady increase in the installed capacity, with 2.5 GW installed in 2022. This is the lowest installed capacity since 2016. However, the total installed capacity still rose to over 30 GW, with The UK (46%), Germany (27%), and The Netherlands (9%) being the biggest contributors.

The average size and capacity of installed wind turbines have stabilized at about 8 MW over the last few years, after increasing steadily until 2020. However, figure 2.3 shows that the average capacity of the turbines ordered has increased drastically since 2019, growing to about 12 MW in 2022, which represents a 50% increase from the average capacity installed in 2022 (WindEurope 2023).

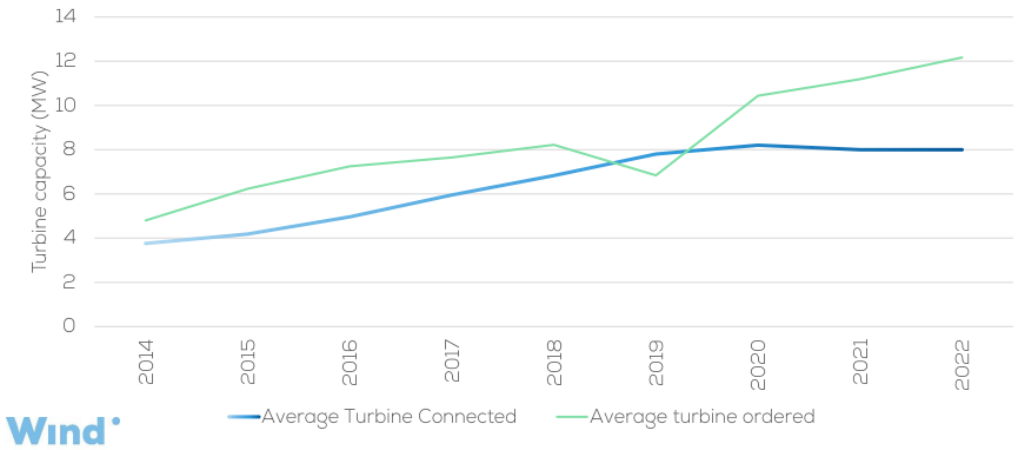

Figure 2.3: Average rated capacity of turbines installed and ordered (WindEurope 2023).

Offshore wind has advantages over onshore wind, such as fewer restrictions on location due to factors such as land availability, wind speeds, transmission access, and wind turbulence. Additionally, offshore turbines can be larger and are located in areas where noise and appearance are not a concern, leading to more power production with less environmental impact (EESI 2016). Today, most offshore wind turbines are bottom-fixed, but advancements in the floating substructure technology over the last decade have provided a higher "technological readiness level" (Du and Paya 2020). Floating substructures are considered to be more economically attractive than bottom-fixed when approaching 50- meters of water depth (Vanelli et al. 2022). It is considered that floating offshore wind can become a significant driver in the energy transition, with 80 % of the offshore wind resources located in waters with more than 60-meter depth, a total potential of over 7000 GW (WindEurope 2017).

Figure 2.4: Floating wind turbines (Hockenos 2020).

2.2 Floating wind structures

As mentioned, most wind turbine substructures today are fixed to the seabed. However, there are several other options, with the tension leg platform (TLP), the semi-submersible, and the spar buoy being the most popular. These are floating structures that are only connected to the seabed through mooring lines. The TLP is restrained by tendon arms connected to anchors on the seabed, allowing lower structural weight and therefore lower material cost. The spar is usually steel or concrete and is stabilized through weight and buoyancy due to a small water plane area and large ballast weight. Finally, the semi-submersible is a free-surface stabilized structure, with a small draft and high flexibility. It is a heavy structure and has high manufacturing complexity (Hopstad et al. 2013).

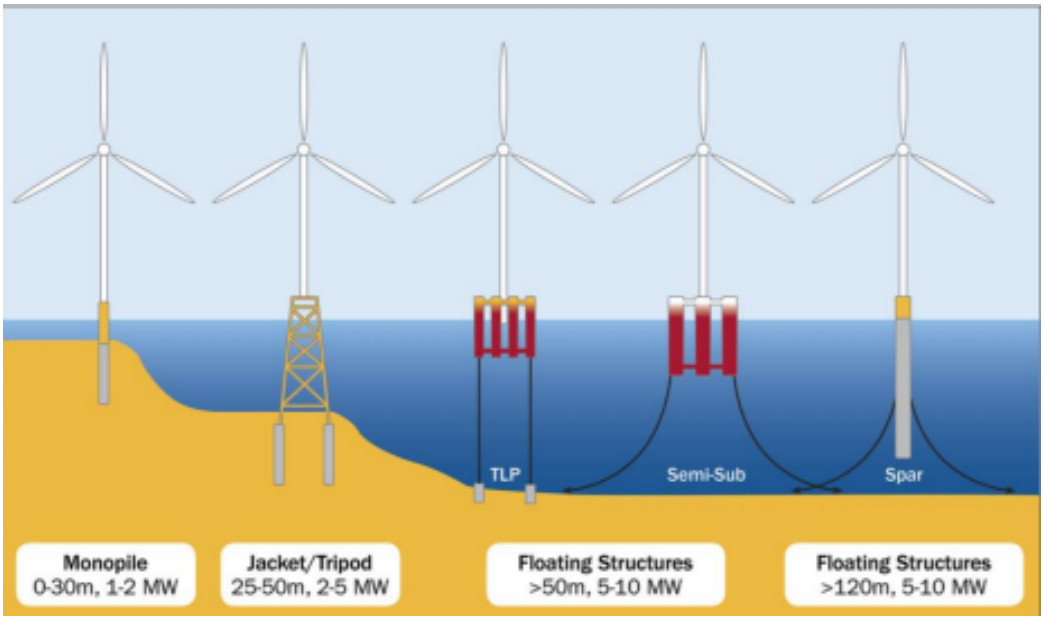

Figure 2.5: Most common offshore wind turbine types (Amdahl and Yu n.d.).

2.3 Floating wind turbines

2.3.1 Hywind Tampen

Hywind Tampen is a floating wind farm located around 140 km from the Norwegian coast, and with a total power capacity of 88 MW, it is the world's largest floating offshore wind farm. It is the first floating wind farm to power offshore gas and oil platforms as it is set to provide electricity for the Snorre and Gullfaks fields in the Norwegian North Sea (Equinor 2022). The farm is made up of eleven turbines upgraded from 8 to 8.6 MW capacity, of which seven are in operation in 2022, while the remaining four will be installed during 2023 (Equinor 2023). The turbines are concrete monopile structures and have a yaw system and an automatic blade-turning system (Equinor 2019)

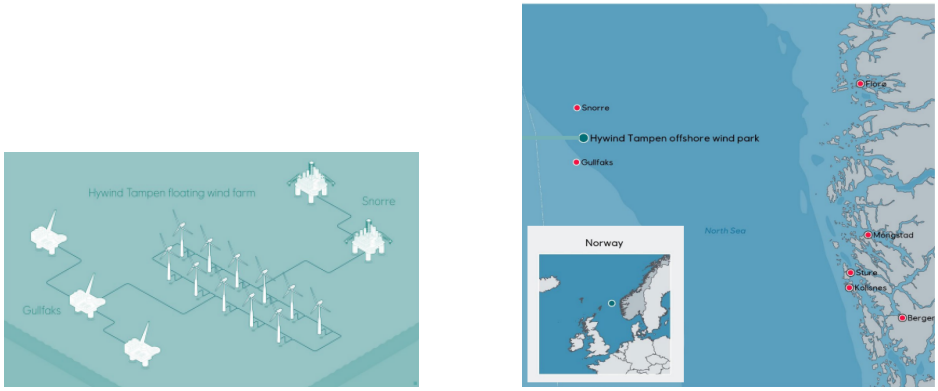

(a) Hywind Tampen connected to Snorre and Gullfaks.

(b) Location of Hywind Tampen, Snorre, and Gullfaks.

Figure 2.6: Hywind Tampen (Hansen 2018).

2.3.2 Traffic density and collision risk around Hywind Tampen

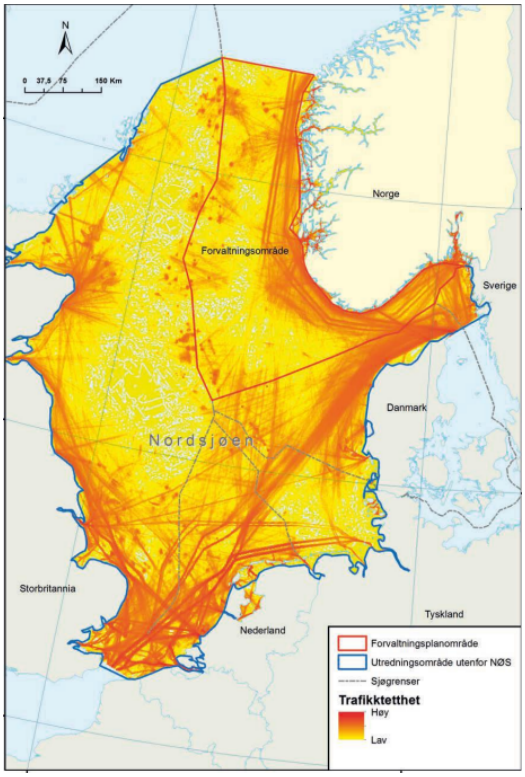

Figure 2.7: Traffic density in the North Sea (Equinor 2019).

Figure 2.7 shows the ship traffic density in the North Sea. It shows that the traffic density is highest around the coast of the surrounding countries and on the English channel. In addition, the density increases around oil reservoirs in the north sea, mainly due to service vessels en route to the platforms. Figure 2.8 shows the density more closely around the Tampen area. It can be seen from the difference of the two figures that the traffic mainly consists of supply and service vessels operating on the installations already existing in this area.

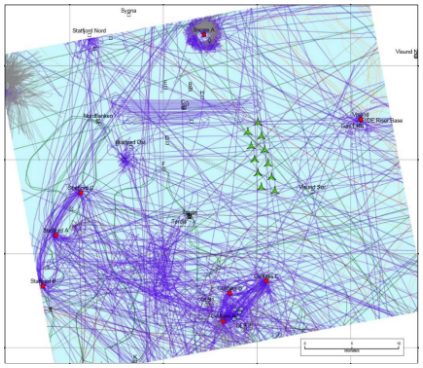

(a) Traffic around the Tampen area for May 2015.

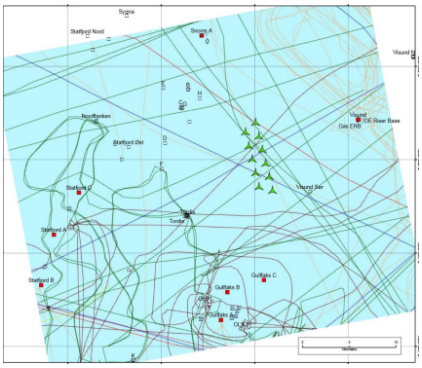

(b) Traffic around the Tampen area for May 2015, disregarding the supply and service vessels.

Figure 2.8: Traffic around the Tampen area for May 2015 (Equinor 2019).

In their impact assessment, Equinor state that the risk of collision with the Hywind wind farm is assumed to be the same as the risk of collision with the nearby platforms Snorre and Gullfaks. For Snorre A, this risk is considered negligible, while for Snorre B it is estimated that the collision frequency is $3 \cdot 10^{-6}$ per year. As for the Gullfaks installations, the collision frequency is estimated as $6.2 \cdot 10^{-6}$ per year. These estimations are all done on the pre-assumption that the traffic in the area is under surveillance and that ships on a collision course are all contacted (Equinor 2019).

2.3.3 Odfjell Oceanwind Deepsea Semi

In 2022 DNV awarded Odfjell Oceanwind with an Approval in Principle (AiP) for the new Deepsea Semi floating wind foundation design. The Deepsea Semi is dimensioned for up to 15 MW wind turbine generators and has been developed for mass production. The foundation covers water depths from 60 to 1300 meters

and includes all areas for floating wind farms in planning in the North Atlantic region as of February 2022. The foundation is optimized for Siemens Gamesa's SG 11.0-200DD and SG 14.0-222DD (M. Andersen 2022). The foundation in shown in figure 2.9.

Figure 2.9: The Deepsea Semi from Odfjell Oceanwind (I. Andersen 2022).

2.3.4 Reference turbine

The Hywind Tampen turbines described in the previous chapter are 8.6 MW turbines, which are the largest floating turbines in operation today. However, wind energy companies are continuously working to increase the size and capacity of the turbines, with some companies having developed turbines with capacities of 15 MW and more (Vestas 2021). Therefore the National Renewable Energy Laboratory (NREL), the Technical University of Denmark (DTU), and the University of Maine have developed a reference turbine that can serve as a baseline for the design of 15-20 MW turbines going forward. The IEA Wind 15-MW is developed for both floating and bottom-fixed substructures. Some of the main dimensions, along with the diameter, thickness, and diameter-to-thickness ratio of the tower are presented in tables 2.1 and 2.2

Parameter	Value
Hub height	150 m
Rotor diameter	240 m
Hub diameter	7.94 m
Number of blades	3
Blade mass	65 t
Rotor nacelle assembly mass	1017 t
Tower mass	860 t
Tower base diameter	10 m
Monopile mass	1318 t

Table 2.1: Main dimensions of the IEA 15 MW reference turbine (Gaertner et al. 2020).

Height [m]	Diameter [m]	Thickness [mm]	D/t [-]
0.000	10.000	45.517	219.698
0.001	10.000	43.527	229.742
5.000	10.000	43.527	229.742
5.001	10.000	42.242	236.731
10.000	10.000	42.242	236.731
10.001	10.000	41.058	243.558
15.000	10.000	41.058	243.558
15.001	10.000	39.496	253.190
28.000	10.000	39.496	253.190
28.001	10.000	36.456	274.303
41.000	9.926	36.456	272.273
41.001	9.926	33.779	293.851
54.000	9.443	33.779	279.552
54.001	9.443	32.192	293.334
67.000	8.833	32.192	274.385
67.001	8.833	30.708	287.645
80.000	8.151	30.708	265.436
80.001	8.151	29.101	280.093
93.000	7.390	29.101	253.943
93.001	7.390	27.213	271.561
106.000	6.909	27.213	253.886
106.001	6.909	24.009	287.767
119.000	6.748	24.009	281.061
119.001	6.748	20.826	324.018
132.000	6.572	20.826	315.567
132.001	6.572	23.998	273.856
144.582	6.500	23.998	270.856

Table 2.2: The thickness and diameter of the reference turbine tower (Gaertner et al. 2020).

Chapter 3

Impact risks and consequences

Floating wind farms have the advantage of operating beyond the water depth considered as maximum for bottom-fixed structures, enabling the exploitation of stronger winds and larger farm sizes located further from shore. This allows us to locate the farms further away from the densest shipping routes, however, it may also present harsher and more challenging conditions. Therefore, the need for service visits may increase, in addition to the fact that the service vessels may need to increase in size (Dai et al. 2013).

There are several activities and operations that may lead to collisions, including:

- Service vessel approaching FOWT.
  - The service vessel fails to stop and hits the FOWT at high speed.
  - The vessel misjudges a turning or maneuvering action and hits the FOWT at relatively low speed.
- Service vessel remains alongside the FOWT performing a task.
  - The vessel loses power and drifts into the FOWT due to wind and waves, at speeds dependent on the conditions.
  - The DP system fails and the vessel drifts into the FOWT due to wind and waves, at speeds dependent on the conditions.

These can be classified into different collision scenarios which need to be analyzed separately and include

- Head-on collision
- Maneuvering collision
- Drifting collision

3.1 Collision consequences

The consequence of impacts between a vessel and a turbine can be divided into three domains.

- Structural damage
- Environmental damage
- Personnel injuries or fatalities

The structural damage range from minor damages to the collapse of the structure and can be classified further, based on the magnitude of the damage.

Magnitude of consequences	**Description**
Not significant	Damage not significant, turbine continues to operate
Considerable	Damage not significant, but turbine stops operating
Serious	Significant damage to turbine
Catastrophic	Wind turbine collapses, large parts fall onto ship deck

Table 3.1: Impact of ship collision on turbine-structure (Presencia and Shafiee 2018).

There are several failure modes that can further describe the consequences of a collision, including:

- The tower collapses and falls either in the direction of the vessel or away from it risking damage to the vessel and injuries to the crew.
- The acceleration of the nacelle exceeds the acceptable limit.
- The blades could be subjected to out-of-plane vibrations, causing them to hit the tower.

- The foundations fail.
- Penetration of empty compartments causing capsizing of the floating structure.

Of these, the first mode with the collapse of the tower onto the vessel is considered the least favorable, as it increases the likelihood of injuries or fatalities (Jørgen Amdahl 2011)

3.2 Accidents

There were 26 reported collisions between platforms and ships on the Norwegian continental shelf between 2001 and 2010, according to the report "COLLISIONS BETWEEN PLATFORMS AND SHIPS IN NORWAY IN THE PERIOD 2001-2010" (Kvitrud 2011). None of the reported accidents resulted in personnel injuries or fatalities, but they did have economic consequences. The report also states that the size of the colliding vessels has increased by about 100 tons per year since 1980 and that since the collision energy increases proportionally with the size of the vessels, the vessels are capable of causing much more damage than they did before.

The report describes the collision between the service vessel Big Orange XVIII and the Ekofisk 2/4 W platform in detail. Big Orange XVIII had been sailing on autopilot which had not been deactivated when entering the safety zone, causing the planned change of course to not occur as expected and the vessel collided with the platform with a speed of 4.8 m/s. This resulted in significant damages to both the vessel and the platform.

According to Kvitrud (Kvitrud 2011) the main causes of the collision could be divided into five different categories

- The safety culture is not good enough in the vessel industry.
- The vessel and equipment become more technical, and the crew is not adequately trained with the new technology.
- There is a high personnel turnover due to a heavy workload and large pay gaps. This means that the crew is often inexperienced.

- The schedule is very tight and leaves little room for recovery for the personnel. In addition, it invites taking chances to keep the routes.
- Short hoses and poor pumping capacity mean the vessel needs to stay close to the platform for a long period of time.

Chapter 4

Design principles

When designing a FOWT, there are several factors that have to be taken into consideration. Due to this, classification societies like DNV and Bureau Veritas have created standards specifically for the design of FOWT structures. These are created to provide guidance, restrictions, and requirements regarding the design and construction of the FOWTs.

4.1 DNV standards

DNV's standards DNV-ST-0119 (DNV 2021b) include the classification of impact loads, specifically for the design of FOWTs. Regarding ship collision, there are two relevant load categories; variable functional loads and accidental loads. Variable functional loads are defined as "loads that may vary in magnitude, position and direction during the period under consideration, and which are related to operation and normal use of the structure in question" including for example impacts from service vessels due to normal operation (DNV 2021b). The design against impacts from vessels shall be based on the largest expected vessel used in regular operation in the wind farm. Impacts from the vessels expected during normal operation shall be accounted for in the ULS, while impacts from drifting vessels due to control failure shall be taken into account in the ALS. In the normal operation scenario, the characteristic impact load shall be the expected maximum from the expected maximum vessel approaching by both bow and stern, during the most severe sea states to be considered for service vessel operation. This includes

a specific speed of no less than 0.5 m/s and the effects of wind, waves, current, and added mass of the vessel. As for the scenario regarding accidental impacts, the characteristics impact load shall be based on the maximum expected vessel during normal operation drifting laterally towards the structure at a specific speed of no less than 2 m/s. In addition, the effects of both added mass and fendering of the vessel shall be taken into account.

The main target of the design against accidental loads is to have a structure where the integrity is not damaged by accidental loads. This can be achieved by either calculating the design accidental loads and verifying that the resistance is not exceeded or by designing the structure as tolerable to accidental loads. This could mean increasing the strength of the structure. Design against the ALS must take two situations into account.

- Resistance check of the structure against design loads.
- Post-damage check of the resistance against environmental loads.

4.2 Bureau Veritas standards

BV's standards NI572 (Veritas 2019) from 2019 also classify impacts from vessels due to normal operation as operational loads. One option is to assess these impacts by dynamic analysis, taking added mass, displacement, sea states, and deformation properties into account. Alternatively, they can be assessed by the prescriptive method where the impact force is given as

$$\mathrm{F_{imp}} = \sqrt{2\mathrm{kE_c}} \tag{4.1}$$

where k is the total spring stiffness at the impact point and E_c is the vessel energy and can be set to

$$\mathrm{E}_c = 0.5\,(\mathrm{M} + \mathrm{M_a})\,\mathrm{V}^2 \tag{4.2}$$

Here, M and M_a are the displacement and added mass of the vessel in tons and V is the maximum approach speed of the vessel in m/s. If this is unknown, the force may be taken as

$$F_{imp} = 2.5M \tag{4.3}$$

Where M is the displacement of the vessel in tons. The ULS corresponds to the maximum load-bearing capacity and includes both ultimate strength and buckling. The ultimate strength shall be checked by the ultimate strength criteria which is that the calculated stresses shall not exceed the allowed stress for the considered loading condition and is given as

$$\sigma_c \leq \sigma_{ALL} \tag{4.4}$$

where σ_{ALL} is the reference stress of the material divided by a safety factor for the given load case. Similarly, the buckling criteria is that the buckling utilization factor η does not exceed the allowed value given as

$$\eta_{ALL} = \frac{1}{SF} \tag{4.5}$$

where SF is the relevant safety factor. The buckling utilization factor is considered the highest ratio between the applied loads and the buckling capacity of the structure. The safety factors for both buckling and strength checks are given in table 4.1

	Load case (A)	**Load case (N)**	**Load case (T)**
Ultimate strength	1.35	1.10	1.5
Buckling	1.5	1.2	1.67

Table 4.1: Safety factors for strength and buckling assessment

Partial safety factors are usually applied on the loads that are applied to the structure. However, the loads like the impact force in a collision are derived from the energy in the collision that has to be dissipated. The energy in the collision is dependent on for example the mass, added mass, and velocity of the structures. Therefore, it may be logical to apply the partial safety factor to the collision energy instead of the collision loads, even though this is not the norm at the moment. The dissipation of energy is described further in the following sections.

4.3 Collision mechanics

The design principles regarding the distribution of strain energy can be distinguished between

- Strength design
- Ductility design
- Shared-energy design

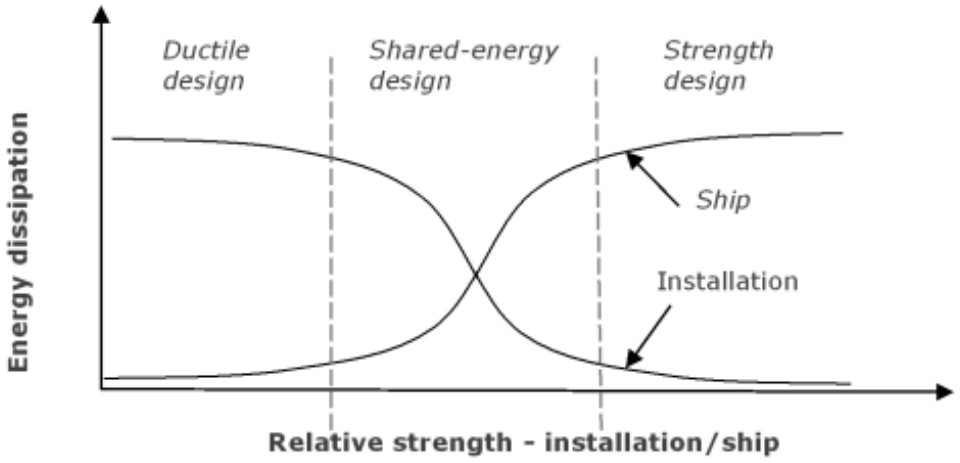

Figure 4.1: Design for energy dissipation (DNV 2021a).

Strength design means that the offshore structure has sufficient strength to resist the collision with little to no deformation, meaning that the ship will deform and dissipate the majority of the strain energy.

Ductility design, on the other hand, implies that the offshore structure is not strong enough to resist the collision and will be subjected to large, plastic deformation and dissipate the major part of the collision energy.

Shared-energy design means the dissipation of the energy will be shared between the ship and the offshore structure, meaning deformation for both structures.

The two first designs are the most favorable when it comes to calculation purposes. This will allow the calculation of the response of the soft structure to be

simplified based on considerations of the rigid structure's geometry. The last, shared-energy design, is more complex. In this case, the magnitude and distribution of the collision force depend on the deformation of both of the structures, and more advanced methods may be needed for accurate estimations. Usually, the transition from ductile to strength design is relatively narrow, meaning that just a small increase in offshore structure strength will lead to a large reduction in its contribution to the dissipation of energy. The most common designs are ductile and shared-energy designs (DNV 2021a).

4.4 Internal and external mechanics

It is common to simplify the problem of ship collision by decoupling the operation into internal and external mechanics (Hong 2009). The external mechanics is used to solve the problem of global rigid body motions and hull girder loads, to then estimate the total energy dissipated by structural deformation. Internal mechanics is used to calculate the structural response of the total energy dissipated and can be represented by the force-deformation relationship. The difference is shown in figure 4.2

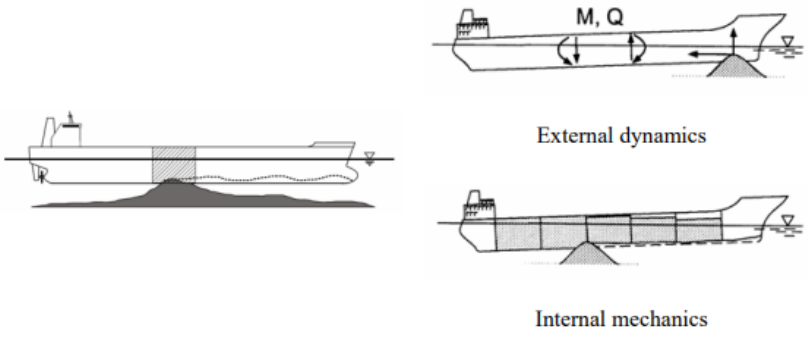

Figure 4.2: Internal and external mechanics of ship grounding (Hong 2009).

4.4.1 External mechanics

The method for calculating the external dynamics proposed by Pedersen and Zhang (Terndrup Pedersen and Zhang 1998) treats the three degrees of motion restricted to the plane of the water surface of both the struck and striking ship. Figure 4.3

shows a local coordinate system with the origin at the impact point and a body-fixed coordinate system with the origin at the center of gravity (CoG) of each ship. The effect of the pressure from the surrounding sea-water is taken into account as virtual added mass. The Lost Kinetic Energy (LKE) is the total energy that should be absorbed by the structural body as deformations and friction during the collision. This is found by solving the force and momentum equilibriums, in addition to the conservation of momentum and energy. The LKE can be represented as

$$LKE = E_\eta + E_\xi \tag{4.6}$$

Where E_η and E_ξ are the LKE in η and ξ direction (Yamada and Pedersen 2007).

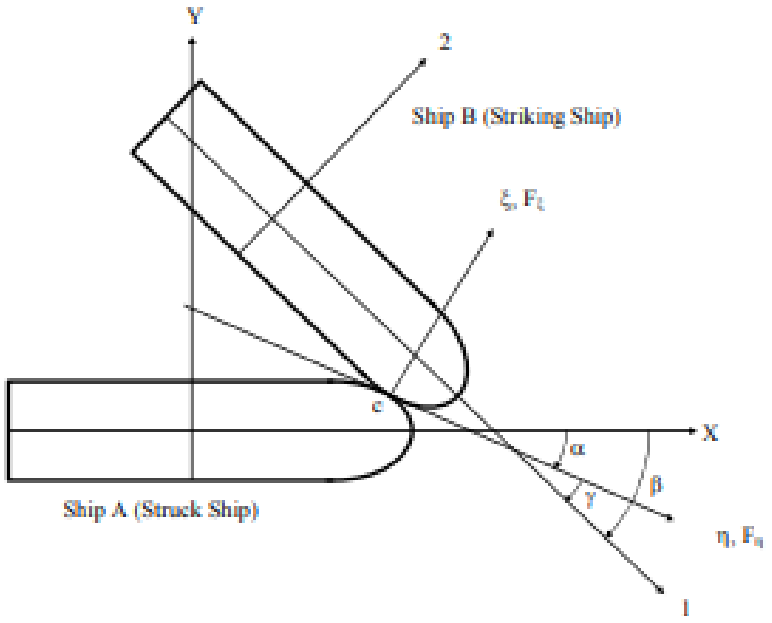

Figure 4.3: Local and body-fixed coordinate system for ship-ship collision analysis (Yamada and Pedersen 2007).

E_η and E_ξ are dependent on the ratio μ between the impulses in η and ξ direction. If μ is lower than a critical value μ_c the bow is assumed to stick to the other ship, and not slide in the η direction, due to the friction force. However, in the other case, where μ is larger than the critical ratio μ_c, the bow will slide in the η direction. This is because the sliding force F_η is larger than the static friction force. E_η and E_ξ can be described as

$$E_\eta = \int_0^{\eta_{\max}} F_\eta d\eta = \frac{1}{2}\frac{\mu}{K_\xi + \mu K_\eta}\dot{\eta}(0)^2 \tag{4.7}$$

$$E_\xi = \int_0^{\xi_{\max}} F_\xi d\xi = \frac{1}{2}\frac{1}{D_\xi + \mu D_\eta}\dot{\xi}(0)^2 \tag{4.8}$$

for the sticking case, and

$$E_\eta = \int_0^{\eta_m} F_\eta d\eta = \frac{1}{2}\frac{\mu_c}{K_\xi + \mu_c K_\eta}\left(\dot{\eta}(0)^2 - \dot{\eta}(T)^2\right) \tag{4.9}$$

$$E_\xi = \int_0^{\xi\,\max} F_\xi d\xi = \frac{1}{2}\frac{1}{D_\xi + \mu_c D_\eta}\left(\dot{\xi}(0)^2 - \dot{\xi}(T)^2\right) \tag{4.10}$$

for the sliding case. Here F_η and F_ξ are impact forces in η and ξ direction. $\dot{\eta}$ and $\dot{\xi}$ are the relative velocities of the ships in the η and ξ direction at the impact point. K_η, K_ξ, D_η and D_ξ are all functions of several parameters including ship mass, moment of inertia, added mass, and impact angle, and T is the time after the collision. A new method has been developed by Zhenhui Liu and Jørgen Amdahl described in "On multi-planar impact mechanics in ship collisions" (Liu and Amdahl 2019) to solve the problem for a full 6DOF + 6DOF system.

4.4.2 Dissipation of energy

As floating platforms such as TLPs and semi-submersibles are considered as compliant structures, the collision energy to be dissipated as strain energy may be taken as

$$E_s = \frac{1}{2}\left(m_s + a_s\right)v_s^2\frac{\left(1-\frac{v_i}{v_s}\right)^2}{1+\frac{m_s+a_s}{m_i+a_i}} \tag{4.11}$$

where:

E_s = strain energy
m_s = ship mass

a_s = ship added mass
v_s = impact speed
m_i = installation mass
a_i = installation added mass
v_i = installation velocity

The velocity of the installation is often set to zero as it is usually relatively stationary (DNV 2021a).

The structural response of the ship and installation can be described by the relationship between load and deformation as shown in figure 4.4. The strain energy dissipated by the respective structures is the total area under the load-deformation curve for the structure and can be described by the following equation.

$$E_s = E_{s,s} + E_{s,i} = \int_0^{w_{s,\max}} R_s dw_s + \int_0^{w_{i,\max}} R_i dw_i \tag{4.12}$$

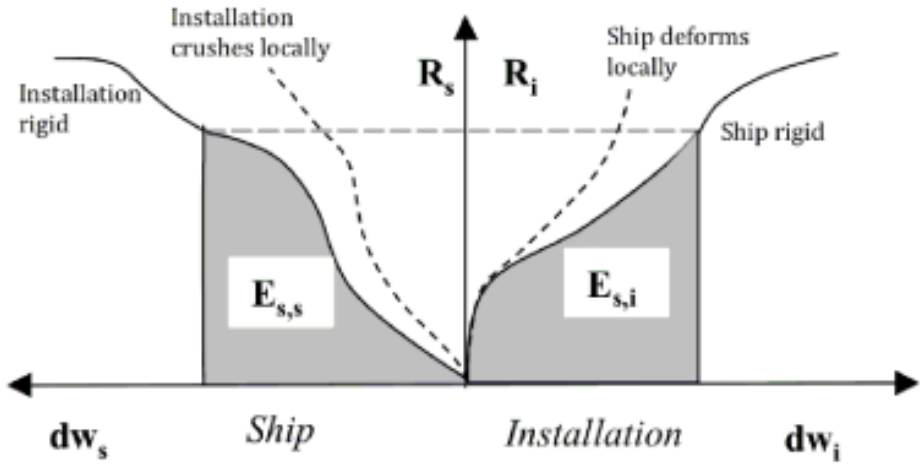

Figure 4.4: Load-deformation curves for ship collision with installation (DNV 2021a).

However, this method has severe limitations. The load-deformation relationship between the two structures is usually established independently of each other, assuming that the other body is infinitely rigid. This means that often the stronger

structure will experience less damage in the analysis than what is actually the case, while it is the other way around for the softer structure, which will often experience more damage than the prediction. This is because the stronger structure's resistance increases as the softer structure's impact force is distributed over a larger area as it deforms. Due to this, a correction factor is introduced, to take the interaction effect into account. The dissipated energy for the two structures can then be described as:

$$E_s = E_{s,s} + E_{s,i} = \beta \int_0^{w_{s,\max}} R_s dw_s + \int_0^{w_{i,\max}} R_i dw_i \tag{4.13}$$

where

$$\beta = \frac{R_c}{R_c^*}, \quad 0 < \beta < 1 \tag{4.14}$$

for impact against tubular members and R_c^* is defined in table 4.2 (DNV 2021a).

Ship type	**Impact type**	**Denting compactness R_c^* [MN]**
Standard OSV with no ice reinforcement	Bulb vertical brace	1.9
	Bulb oblique brace	1.4
	Stern corner	1.0
	Side/stern end	1.2
Standard OSV with ice class ICE-C	Bulb or stern	3.2
	Side	2.3
V-shaped bow with ice class ICE-C	Bow on brace	3.5
	Leg and vertical brace	4.3
Other bow configurations	Bow on brace	$R_c^* = 1.9 \frac{F_{\max}}{24}$
F_max = peak collision force if this occurs within 2 m deformation.		

Table 4.2: Denting compactness for different OSV types (DNV 2021a).

4.5 Ship collision forces

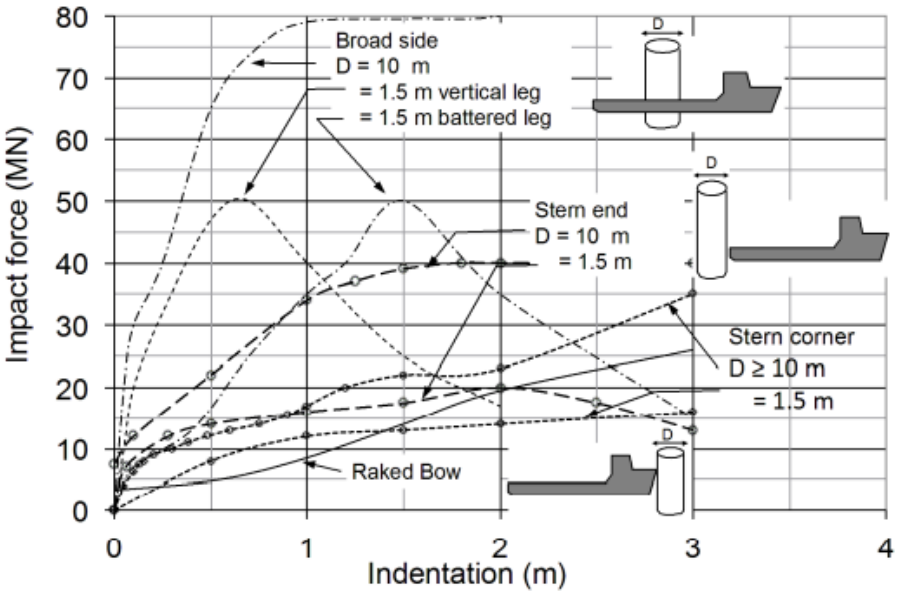

Figure 4.5: Recommended force-deformation curve (DNV 2021a).

Figure 4.5 shows the force-deformation relationship for broadside, bow, stern end, and stern corner impacts for standard supply vessels with displacement between 6500 and 10000 tons. The curves for broadside, stern end and stern corner impacts are based of penetration of an infinitely rigid cylinder, while the curve for bow impact is based on impact with an infinitely rigid plane wall. Therefore the bow-impact curve is only applicable for plane walls or large-diameter columns, and not for for example collisions against tubular braces.

4.6 Force-deformation relationship of tubular members

Local deformation may, depending on the slenderness of the cross-section and the area of contact, occur for a tubular member, and will typically happen in the form of a dent. This has two effects; firstly, during the denting process energy will be

dissipated. Secondly, the dent will reduce the bending capacity of the section, causing additional bending moments from the axial force through the eccentricity created in the damaged section. However, the effects on energy dissipation are usually only significant for jacket legs as the contribution from the brace members is often small, and can be neglected.

Regarding energy dissipation due to denting, the true geometry obtained through experiments is presented in figure 4.6 and 4.7. This shows a flattened part in the cross-section which has reduced effectiveness which is assumed to be in the central contact area which is the area that is in direct contact with the colliding structure, in this case, the ship. This part transitions to an undamaged part through decreasingly flattened, triangular regions. The other part is undamaged and virtually unaffected by the deformation. The virtual work principle is used to assess the deformation resistance, taking the change of curvature and the plastic rotation contribution into account (Skallerud and Amdahl 2002)

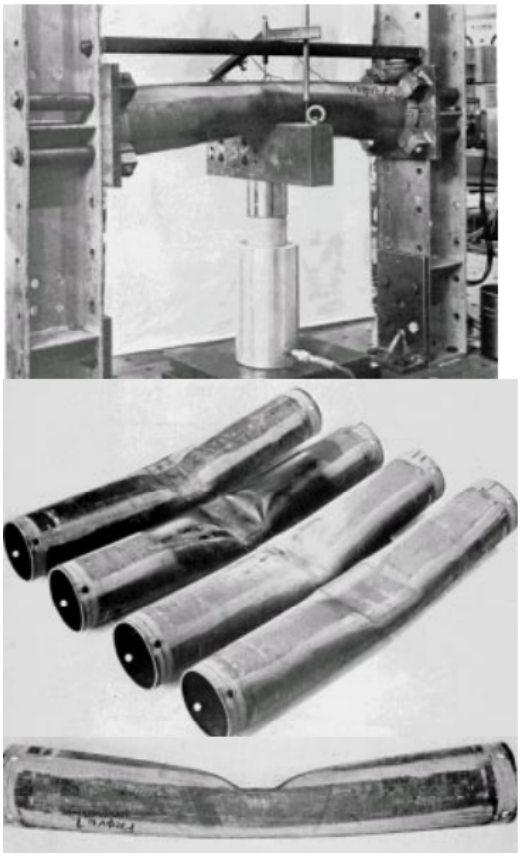

Figure 4.6: Local denting experiments (Skallerud and Amdahl 2002).

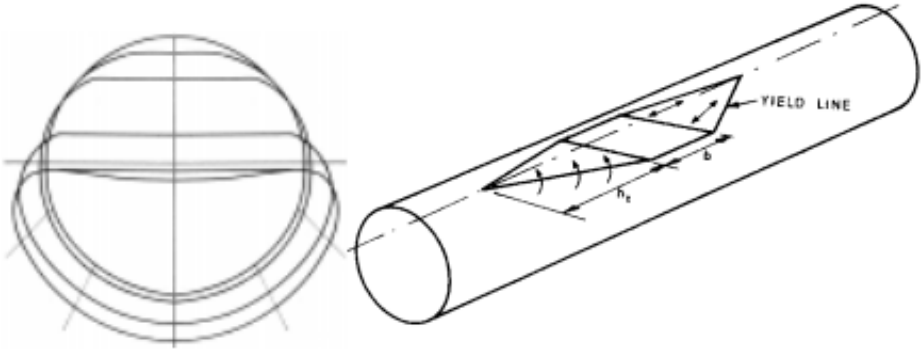

Figure 4.7: Model of the true geometry of the deformed cross section (Skallerud and Amdahl 2002).

Figure 4.8 shows the relationship between resistance to indentation of unstiffened tubes and the indentation of the tube itself. These are based on plastic analysis and are developed on non-dimensional form.

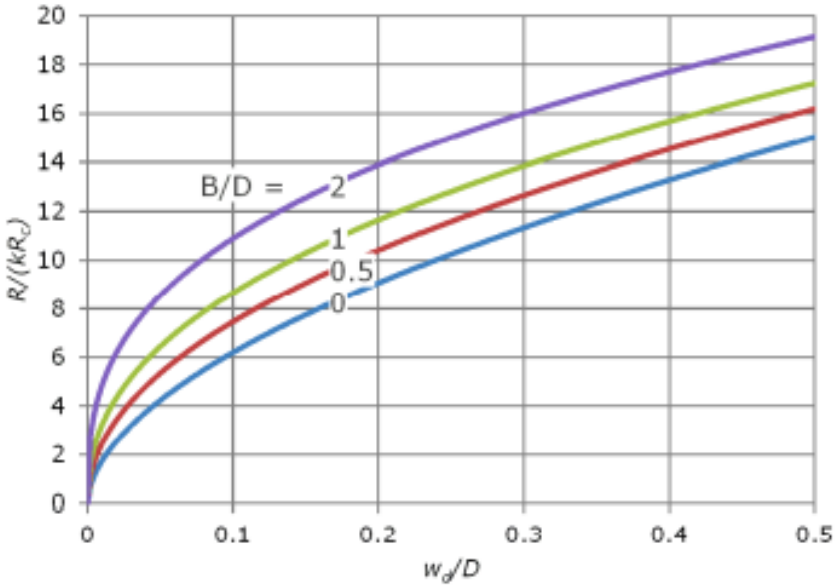

Figure 4.8: Resistance curve for local denting (DNV 2021a).

The resistance may be taken from the figure or may be calculated from the equation

$$\frac{R}{R_c} = kc_1 \left(\frac{w_d}{D}\right)^{c_2} \quad \text{for: } \frac{w_d}{D} \leq 0.5 \tag{4.15}$$

where

$$\begin{aligned} R_c &= f_y \frac{t^2}{4}\sqrt{\frac{D}{t}} \\ c_1 &= 22 + 1.2\frac{B}{D} \\ c_2 &= \frac{1.925}{3.5 + \frac{B}{D}} \end{aligned} \tag{4.16}$$

and

$$k = \begin{cases} 1 & \text{if } \frac{N_{Sd}}{N_{Rd}} \leq 0.2 \\ 1 - 2\left(\frac{N_{Sd}}{N_{Rd}} - 0.2\right) & \text{if } 0.2 < \frac{N_{Sd}}{N_{Rd}} < 0.6 \\ 0 & \text{if } \frac{N_{Sd}}{N_{Rd}} \geq 0.6 \end{cases} \tag{4.17}$$

N_{sd} = design axial compressive force
N_{Rd} = design axial compressive resistance
B = width of contact area
w_d = dent depth
D = diameter of tubular member
t = thickness of tubular member

However, these curves are not accurate for small indentations ($w_d/D < 0.05 - 0.1$) and should therefore not be used in designs where the dents are required to be within that region (DNV 2021a).

These resistance curves are based on collision between a tubular member and the side of a ship, making the width of the contact area, B, the height of the plane section of the ship side under consideration. Depending on the width of the contact area and the relative rigidity of the cross-section and the ship side it may also be inaccurate to assume that the tubular member is flattened over the entire contact area.

According to i report written by Icaro Ladeira from Nantes University (Ladeira

2022) another way of describing the force-displacement relationship is presented in equation 4.18

$$P_{el} = 2.083Et\left(\frac{t}{R}\right)^{1.22}\left(\frac{R}{L}\right)^{0.5} w_l \tag{4.18}$$

Here P_{el} is the elastic local resistance, w_l is the local indentation, t is the thickness, R is the radius, L is the length of the tubular member and E is the elastic modulus. According to the report, this is accurate for tubes with an L/D ratio of over 9.

4.7 Buckling of cylinders

Both stiffened and unstiffened shells are important elements in offshore structures. This is for example represented in the tower and columns of the wind turbine. They are often subjected to both compressive stresses and moments, due to for example the weight of the nacelle and rotors and the thrust force in the case of the wind turbine. Therefore it is important that they are designed against buckling criteria (Amdahl 2005). In addition, collisions between the turbine and vessels may cause structural damage to the turbine structures, and deformations may decrease its resistance to buckling.

Figure 4.9 shows a theoretical load-end shortening curve for cylindrical shells that are subjected to axial compression. It shows that initially, the structure will follow a linear primary equilibrium path, but at some point, an unstable secondary path, with a different buckling mode, intersects with the primary path. This is called the bifurcation point and is seen in point B. This is, however, rarely reached in practice, due to imperfections in the shell which cause the cylinder to fail at a smaller load, which is represented by the limit point L.

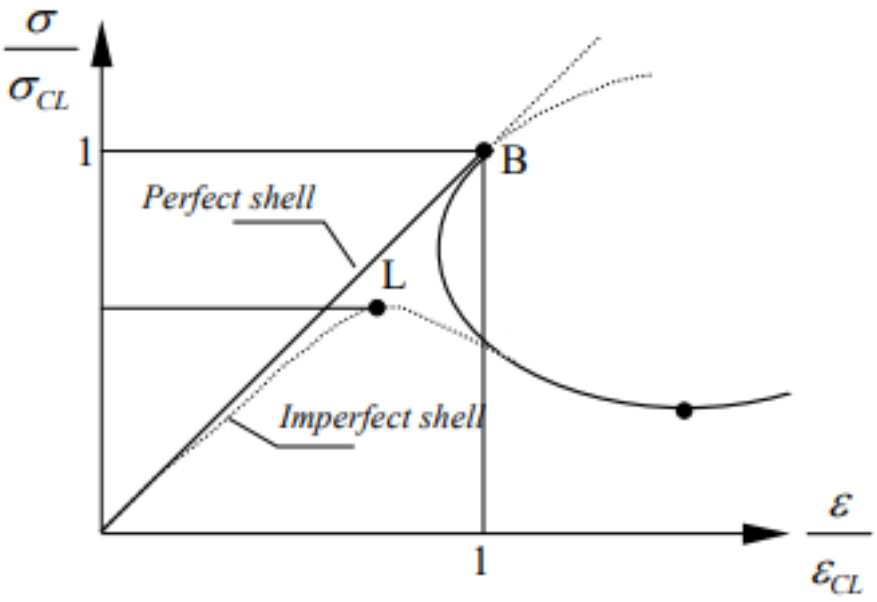

Figure 4.9: Equilibrium paths for perfect and imperfect shells (Amdahl 2005).

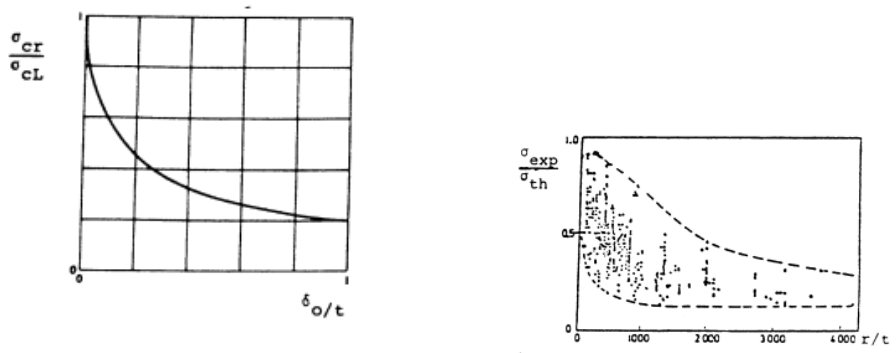

(a) Result of axisymmetrical imperfection on buckling load.

(b) Experimental results for buckling loads.

Figure 4.10: Buckling loads (Amdahl 2005).

Figure 4.10a shows the influence of an axisymmetrical initial imperfection, δ_0, on the buckling load. As seen in the figure, just a small imperfection of 1/10 of the wall thickness can reduce the buckling load to 60% of the theoretical value. This sensitivity to imperfections is also shown in figure 4.10b which is a plot of experimental buckling loads. Due to this sensitivity, cylindrical shell design is

based on modification of the theoretical load by an empirical reduction known as the knock-down factor (Amdahl 2005).

4.7.1 Axial compression

Axial compression can come from the weight of the nacelle and blades. This will create an axial compression force. Assuming:

$$N_x = \frac{P}{2\pi r}, \quad N_{x\theta} = N_\theta = 0 \tag{4.19}$$

gives the equation for the critical stress

$$\sigma_{xE} = \frac{\pi^2 E}{12\left(1-v^2\right)}\left(\frac{t}{l}\right)^2\left[\frac{\left(m^2+\bar{n}^2\right)^2}{m^2}+\frac{12Z^2}{\pi^4}\frac{m^2}{\left(m^2+\bar{n}^2\right)^2}\right] \tag{4.20}$$

where

- m is the number of half waves in the longitudinal direction
- n is the number of entire waves in circumferential direction
- Z is the Batdorf parameter

$$Z = \frac{l^2}{rt}\sqrt{(1-v^2)} \tag{4.21}$$

-

$$\bar{n} = \frac{nl}{\pi r} \tag{4.22}$$

Minimizing equation 4.20 to find the smallest critical stress will ultimately give the equation for the critical load

$$\sigma_{xE} = \frac{C\pi^2 E}{12\left(1-v^2\right)}\left(\frac{t}{l}\right)^2 \tag{4.23}$$

where C represent a buckling coefficient.

$$C = \frac{4\sqrt{3}}{\pi^2} Z \tag{4.24}$$

4.7.2 Buckling due to bending

Buckling may also occur due to the bending moment caused by the thrust force from the wind on the rotor. This is much more difficult to analyze for cylinders due to two different causes. Firstly, the stress distribution is not constant around the circumference of the cylinder. Secondly, this is because of the fact that due to the cross-section being ovalized, the pre-buckling deformations of long cylinder are no longer linear. However, studies show that for all practical purposes, the buckling resistance due to bending may be considered as equal to the buckling stress due to axial compression, as described in the previous section (Amdahl 2005).

4.7.3 Buckling of imperfect shells

Conventional buckling theory as described in the previous chapter is generally only valid for idealized structures. However, there are two main effects that have a damaging effect on the real buckling load of cylindrical shells.

- Material imperfections
- Shape imperfections

While material imperfections, like residual stresses and heterogeneities mainly affect the elasto-plastic range of buckling, shape imperfections affect both the elastoplastic and the elastic range. To take the shape imperfections into account the fore-mentioned knock-down factor is introduced to reduce the elastic buckling resistance.

$$\sigma_E = \rho \sigma_{cl} \tag{4.25}$$

where ρ is the knock-down factor and σ_{cl} is the classical elastic buckling resistance. The buckling coefficient can in general be represented by the expression

$$C = \psi \sqrt{1 + \left(\frac{\xi}{\psi}\right)^2} \tag{4.26}$$

where ψ is the buckling coefficient for a plane plate, and ξ represents the contribution from the curved shell. While plates are not very sensitive to shape imperfections, as described earlier this is not the case for curved shells. Therefore the knock-down factor is only applied to the contribution of the curved shell, and the coefficient becomes:

$$C = \psi \sqrt{1 + \left(\frac{\rho\xi}{\psi}\right)^2} \tag{4.27}$$

The influence of the shape imperfection factor is shown in figure 4.11 (Amdahl 2005).

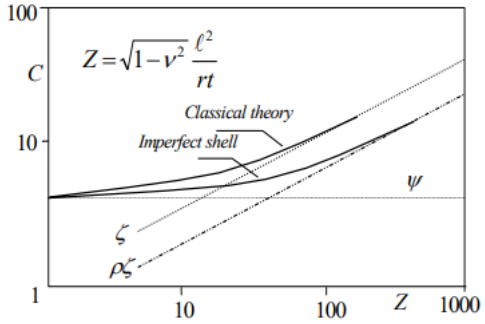

Figure 4.11: Effect of imperfection factor on buckling load (Amdahl 2005).

The buckling coefficients for an unstiffened cylindrical shell due to axial stress and bending is presented in table 4.3. As mentioned, for practical purposes buckling due to bending and axial stress is considered equal.

	ψ	ξ	ρ
Axial stress	1	0.702Z	$0.5(1+\frac{r}{150t})^{-0.5}$
Bending	1	0.702Z	$0.5(1+\frac{r}{150t})^{-0.5}$

Table 4.3: Buckling coefficients for an unstiffened cylindrical shell (Amdahl 2005).

The bending capacity of a dented tubular member is considered in DNV RP C204 (DNV 2021a). The reduction in plastic bending moment capacity is described as

$$\begin{aligned} \frac{M_{\text{res}}}{M_p} &= \cos\frac{\theta}{2} - \frac{1}{2}\sin\theta \\ M_p &= \sigma_y D^2 t \\ \theta &= \arccos\left(1 - 2\frac{w_d}{D}\right) \end{aligned} \tag{4.28}$$

Where M_p and M_{res} are full and residual plastic bending moment capacity. The reduction of moment capacity due to local dents is also shown in figure 4.12.

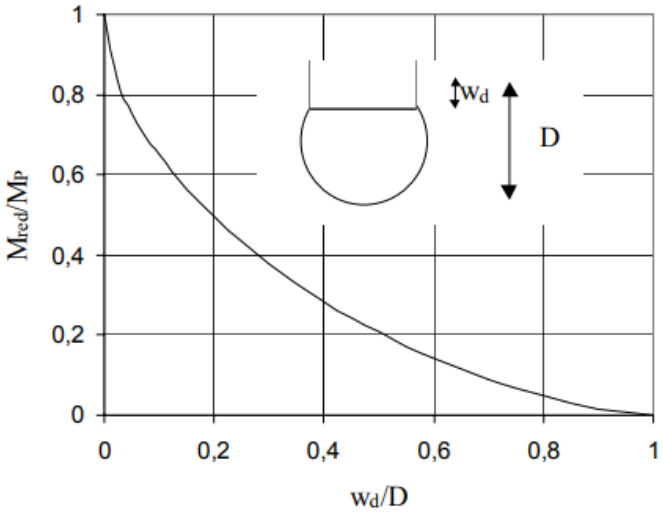

Figure 4.12: Reduction of moment capacity due to local dent (DNV 2021a).

Chapter 5

LS-DYNA software

LS-DYNA is a general-purpose FE code used for analyzing the large deformation dynamic and static response of structures (LS-DYNA 2022). The main solution methodology is based on explicit time integration and uses a modification of the central difference scheme to integrate the equations of motion (LS-DYNA-Support 2023b). In LS-DYNA's modification of the central difference scheme, the semi-discrete equations of motion at time n are given as

$$\mathbf{M}\mathbf{a}^n = \mathbf{P}^n - \mathbf{F}^n + \mathbf{H}^n \tag{5.1}$$

where $\mathbf{M}$ is the diagonal mass matrix, $\mathbf{P}^n$ accounts for the external and body force loads, $\mathbf{F}^n$ is the stress divergence vector and $\mathbf{H}^n$ is the hourglass resistance. To find the next timestep t^{n+1} central difference time integration is used. Equation 5.1 is used to find the expression for the acceleration $\mathbf{a}^n$ at timestep n.

$$\mathbf{a}^n = \mathbf{M}^{-1}\left(\mathbf{P}^n - \mathbf{F}^n + \mathbf{H}^n\right) \tag{5.2}$$

The global nodal velocity and displacement vectors are given as

$$\mathbf{v}^{n+1/2} = \mathbf{v}^{n-1/2} + \mathbf{a}^n \Delta t^n \tag{5.3}$$

and

$$\mathbf{u}^{n+1} = \mathbf{u}^n + \mathbf{v}^{n+1/2}\Delta t^{n+1/2} \tag{5.4}$$

respectively, where

$$\Delta t^{n+1/2} = \frac{\left(\Delta t^n + \Delta t^{n+1}\right)}{2} \tag{5.5}$$

Then, the geometry is updated by adding the displacement increments to the initial geometry

$$\mathbf{x}^{n+1} = \mathbf{x}^0 + \mathbf{u}^{n+1} \tag{5.6}$$

Although this requires more storage to store the displacement vector, the sensitivity to round-off error is much smaller. The stability condition of this method is given by

$$\Delta t_{cr} \leq \frac{2}{\omega_{\max}} \tag{5.7}$$

where $\omega_{\max}$ is the largest natural frequency.

Chapter 6

Structural modeling for collision analyses

The collision analyses are made up of several models. There is one model for the tower section and several models for the different parts of the ship colliding with the tower section which are all described in this section. Supervisors Jørgen Amdahl and Zhaolong Yu handed out the different ship models, while the tower section was created in LS-DYNA Preprost.

6.1 Tower model

The main dimensions of the tower model are presented in table 6.1. The tower represents the Deepsea Semi from Odfjell Oceanwind presented in figure 2.9. An Usfos model received from supervisor Jørgen Amdahl of the entire structure is shown in figure 6.1. The lower part of the tower has a 12-meter diameter with 25 mm thickness and ring stiffeners, which is modeled in the tower section in LS-DYNA. To simplify the model, the cone transitioning the tower-diameter from 12 to 8 m is not considered, and the tower therefore has a constant diameter. These main characteristics give a diameter-to-thickness ratio of almost 500. This is way above what is proposed in the reference turbine from IEA presented in table 2.2, where the maximum ratio is just above 300. However, ring-stiffened cylinders often have large diameters and high diameter over thickness ratios (Yu and Amdahl 2018). In addition, due to the ring stiffeners an equivalent thickness of 37.5 mm

has been established, described in section 8.3.1. This equivalent thickness would give a diameter-to-thickness ratio of 320, which is in line with what is seen in the reference turbine.

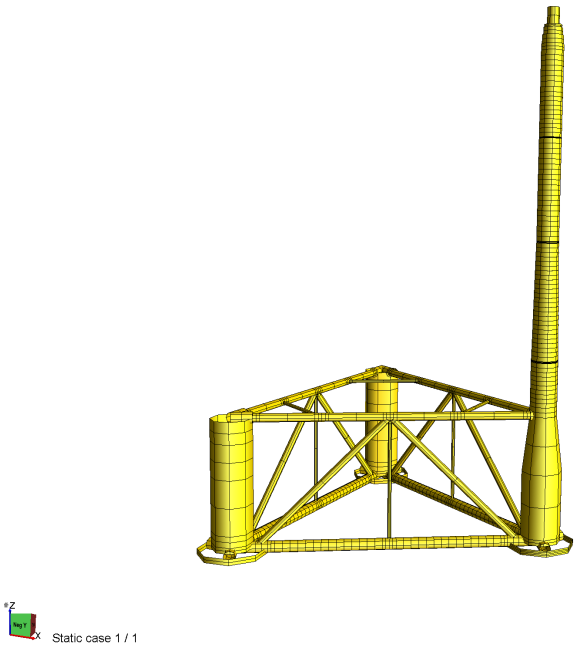

Figure 6.1: Usfos model of the Odfjell Oceanwind Deepsea Semi structure.

Parameter	**Value**
Diameter [m]	12
Height [m]	16
Thickness [mm]	25
Stiffener spacing [m]	1
Stiffener thickness [mm]	25

Table 6.1: Main dimensions of tower section.

The material used for the tower model is the implemented material *MAT_018_POWER_LAW_PLASTICITY which is an elastoplastic material assuming a power law hardening rule and uses the Cowper and Symonds model to include the strain rate effects (Fimreite 2022). Equation 6.1 gives the constitutive relation of the material. The material parameters n and k describe the plastic hardening, ε_{yp} is the elastic strain until the first yield and C and p are strain effect

parameters. ε^{-p} is the effective plastic strain and $\dot{\varepsilon}$ is the strain rate (LS-DYNA 2017). The material parameters are presented in table 6.2

$$\sigma_y = k\left(\varepsilon_{yp} + \vec{\varepsilon}^{p}\right)^n \left(1 + \left(\frac{\dot{\varepsilon}}{C}\right)^{1/p}\right) \tag{6.1}$$

Parameter	Value
Density [kg/m^3]	7850
Young's modulus [GPa]	204
Poisson's ratio [-]	0.3
Initial yield stress [MPa]	338
K [MPa]	758
n [-]	0.19

Table 6.2: Material parameters of the tower model.

6.2 Vessel model

The models are based on a typical modern supply vessel with a displacement of 7500 tons. The main dimensions are presented in table 6.3.

Parameter	Value
Displacement [ton]	7500
Length [m]	91
Length between perpendiculars [m]	79
Breadth [m]	18.8
Depth [m]	7.6
Draft [m]	6.2

Table 6.3: Main dimensions of vessel (Amdahl and Yu 2018).

The material used for all the different vessel models is the same material, *MAT_018_POWER_LAW_PLASTICITY, as described for the tower section model. However, the material properties are different, and presented in table 6.4. The models are described in the following sections, with more detailed information given in the Section C.

Parameter	Value
Density [kg/m^3]	7850
Young's modulus [GPa]	206
Poisson's ratio [-]	0.3
Initial yield stress [MPa]	275
K [MPa]	740
n [-]	0.24

Table 6.4: Material parameters of the vessel models.

6.2.1 Bow model

The bow model is based on the mentioned supply vessel and is shown in figure 6.2. The element size in the bow model is generally 120 mm, with plate thickness varying from 7.5 mm to 12.5 mm for the deck and bulb, and up to 15 mm for the ring stiffener and breast hooks. The stiffener spacing is approximately 600 mm. The bulb is almost cylindrical and relatively strong. The forecastle protrudes 1.2 m ahead of the bulb (Amdahl and Yu 2018).

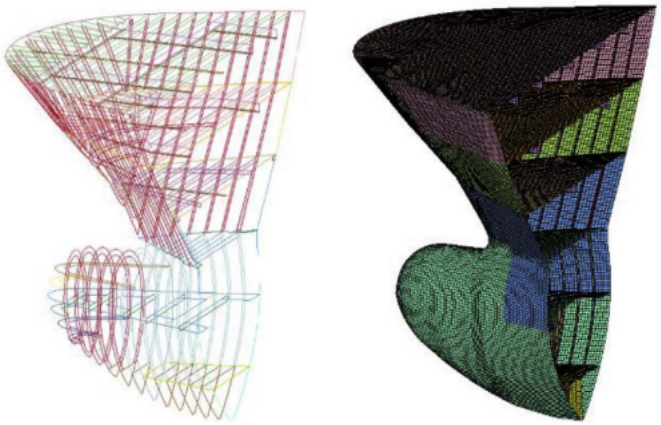

Figure 6.2: Model of the bow section (Amdahl and Yu 2018).

6.2.2 Stern corner model

The stern corner model is based on the same supply vessel as the bow model with main dimensions in table 6.3. The model is half of a stern end, modeled specifically for stern corner collisions, and is shown in figure 6.3. The model has a narrow vertical section, measuring 0.6 m at the corner and 0.83 m at the stern end. The length of the model is 8.1 m, ensuring that the energy absorption is sufficient while still not violating the boundary conditions. The outermost plate has a thickness of 11 mm, while the deck plate has a thickness of 15 mm. Transverse and longitudinal frames are positioned with a distance of 0.65 m between them, and have a plate thickness of 10 or 15 mm. The mesh size is generally 10 cm giving an element size over shell thickness ratio ranging from 5 to 10 (Amdahl and Yu 2018).

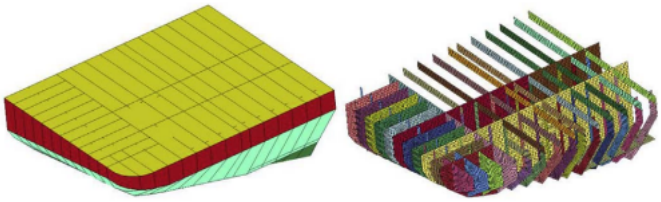

Figure 6.3: Model of the stern corner (Amdahl and Yu 2018).

6.2.3 Shipside model

The side of the supply vessel is also modeled, in order to analyze a collision between the tower and the shipside. The model is shown in figure 6.4. The model has a height, length, and width of 7.6 m, 15.6 m, and 5.5 m respectively. The thickness varies from 7.5 to 25 mm, with the side girders in the bilge area being 9.5 mm with 650 mm spacing (Amdahl and Yu 2018).

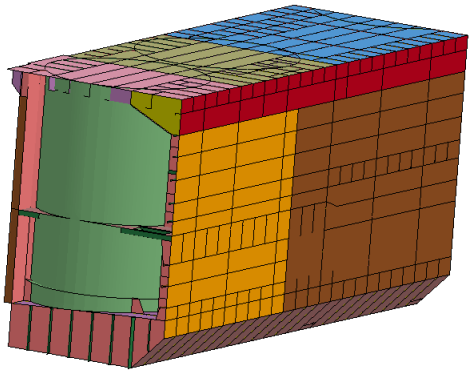

Figure 6.4: Model of shipside.

6.3 Collision modelling

The collision is accomplished by giving the top and bottom end of the tower a prescribed motion toward the vessel with a constant speed of 5 m/s. The speed is set after discussions and agreed upon with the supervisor. The tower ends are free to translate only in the motion direction and fixed for translation in other directions in addition to rotations. For the bow collision, the back end of the bow model is fixed for all degrees of motion. As for the stern corner collision the two sides opposite the tower, representing the inside of the vessel, are fixed for all degrees of freedom, while the side collision model is fixed for all degrees of freedom on the sides and backside.

The contact between the vessel and the tower is modeled using the contact type *CONTACT_AUTOMATIC_SURFACE_TO_SURFACE which treats penetration for both surfaces. In addition, it is recommended to include the self-contact within the models in crash analyses, which is done by using the contact type *CONTACT_AUTOMATIC_SINGLE_SURFACE. The contact friction coefficient was set to 0.3.

Chapter 7

Mesh size convergence study

In finite element analyses, there are several factors that can affect the accuracy of the results. One of them is the size of the elements in the mesh of the structure. A finer mesh usually means higher accuracy of the results, but may also drastically increase the computational resources needed to perform the analysis. Therefore, a mesh size convergence study can be used to find a satisfactory balance between accuracy and computational time. In this chapter, the effects of decreasing the mesh size will be looked at, in order to see how much it will affect the results. The vessel and tower are described in chapter 6 and the tower is meshed with element sizes of 20, 10, and 5 cm.

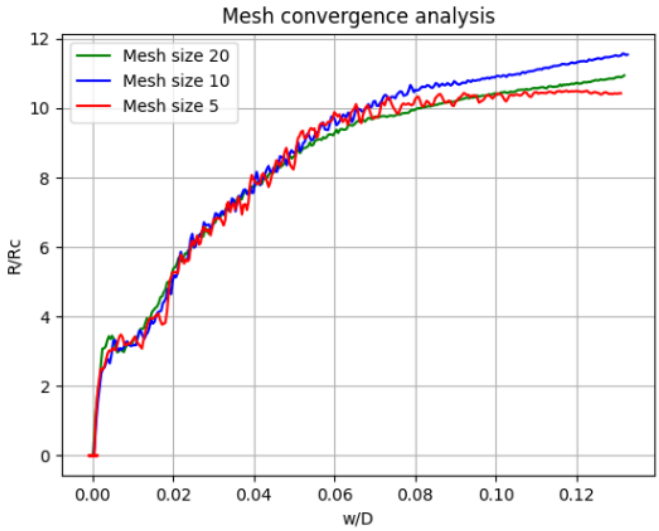

Figure 7.1: Mesh size convergence test.

Figure 7.1 shows the results from the analyses of the collision for the three different mesh sizes of 20, 10, and 5 cm. The plots show that the analyses agree quite well even for different mesh sizes and that there are few significant differences. There are, however, a few notable aspects in the results. Firstly, the most noticeable deviation comes in the later phase of the analyses, where it can be seen that the results have a larger span and that the largest and smallest mesh sizes seem to agree more with each other than with the 10 cm mesh size. Secondly, there is a dip in the increase of resistance force in the early phase of the collision. This represents the initial contact and will be discussed further in section 8.1. This is the case for all mesh sizes, however, there is higher compliance between the two smaller mesh sizes, as the results from the large-mesh analysis show a later, and more significant dip in the increase rate, while the two smaller have earlier and smoother dips. This is shown more clearly in figure 7.2.

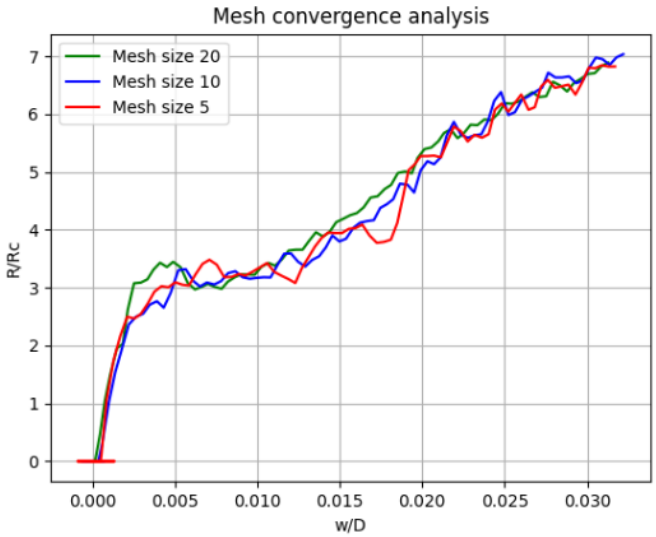

Figure 7.2: Mesh size convergence test zoomed.

As there are few significant differences in the analyses for the different mesh sizes, the decision is to move further with the mesh size of 10 cm. This is because it saves computational resources and time compared to the smaller mesh size, while still complying well. The reason not to choose the largest mesh size to save even more computational resources is that while there is still a good agreement in the results, the two smaller mesh sizes seem to agree closer to each other, especially for small indentations, which is the main focus of this thesis.

Chapter 8

Impact analyses

8.1 Bulb collision

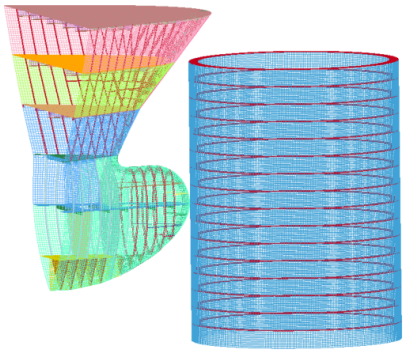

Figure 8.1: Bulb collision model.

The model for the bulb collision is shown in figure 8.1. The full model is made up of the ship bow model as described in chapter 6.2.1 while the tower is the model described in Section 6.1, with a 10 cm mesh size.

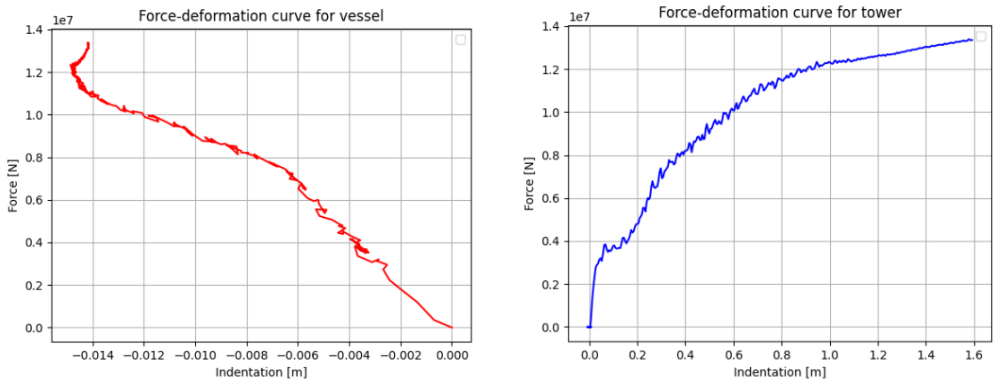

(a) Force-deformation curve for the vessel bow.

(b) Force-deformation curve for the tower section.

Figure 8.2: Force-deformation curves.

Figure 8.2 shows force-deformation curves for the tower and vessel for the bulb collision scenario. It can be seen from figure 8.2a that the bulb dissipates very little of the energy from the collision as the deformation of the bulb is less than 2 cm, and that the resistance force increases to about 13 MN for the small deformation. As for the tower, the deformations are much larger. The deformation in the tower increases quickly with the impact force uptil a value of 13 MN.

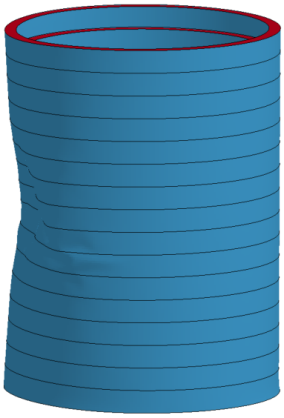

Figure 8.3: Deformation of the tower section.

8.1.1 Discussion

While the force-deformation curve for the tower increases quite steadily, there is an initial peak representing the first impact between the structures. After this, there is a small dip in the slope of the curve, before it starts increasing steadily again. One possible reason for this is that the contact area becomes larger, which both distributes the impact force over a larger area and also engages more stiffeners in the contact area. The deformations in the tower can be seen in figure 8.3, while the deformation of the bulb is almost unnoticeable but presented in Section A.1.

8.2 Forecastle collision

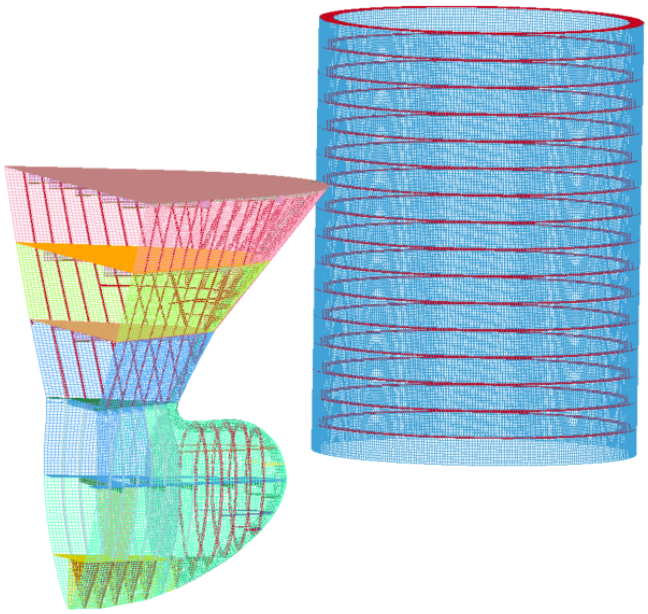

Figure 8.4: Forecastle collision model.

For the forecastle-tower collision, the same model as for the bulb-tower collision is used. However, in this collision, the tower section is translated vertically to collide with the forecastle, and the contact definition described in chapter 6.3 is

changed from the bulb to the forecastle. As opposed to the bulb collision, the collision between the tower and the forecastle of the vessel resulted in large deformations in the forecastle and only small deformations in the tower. Figure 8.5 shows the force deformation curves of the tower and the forecastle. Figure 8.5b shows that the tower will dissipate most of the energy in the initial phase of the collision. The collision force increases almost linearly with the deformation of the tower up to about 6 MN, where the tower has deformed almost 25 cm. After this, the resistance in the vessel decreases significantly, and the vessel starts dissipating all the energy in the collision.

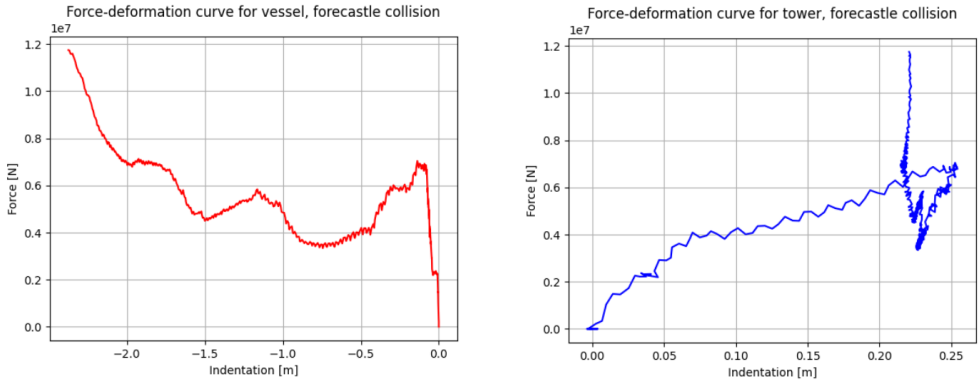

(a) Force-deformation curve for the forecastle.

(b) Force-deformation curve for the tower section.

Figure 8.5: Force-deformation curves.

8.2.1 Discussion

The force-displacement curve for the tower in the collision with the forecastle follows a similar path as the one for the bulb collision presented in figure 8.2b in the early phase of the collision while the collision force is below 6 MN. At this point, the vessel starts dissipating the energy. The significant drop in the resistance of the forecastle may be due to the integrity of the center stiffening plate being compromised as it deforms. This deformation can be seen in figure 8.6 with the von Mises stress plotted. It shows that both the stress area and the intensity increase in the two pictures. As the forecastle extends 1.2 meters in front of the bulb, the collision between the forecastle and the tower may be compared to the collision with a raked bow in the recommended force-displacement curves in figure 4.5 for the first 1.2 meters of displacement. This comparison shows that the curves share some characteristics. The resistance increases drastically until 6 MN, before the

resistance decreases in the simulation, while for the recommended curves, even though the increase rate is significantly reduced, the resistance never decreases. This means that the recommended curves will overestimate the resistance after the initial phase of the collision. This may be because the bulbous bow may differ from raked bows also in the forecastle.

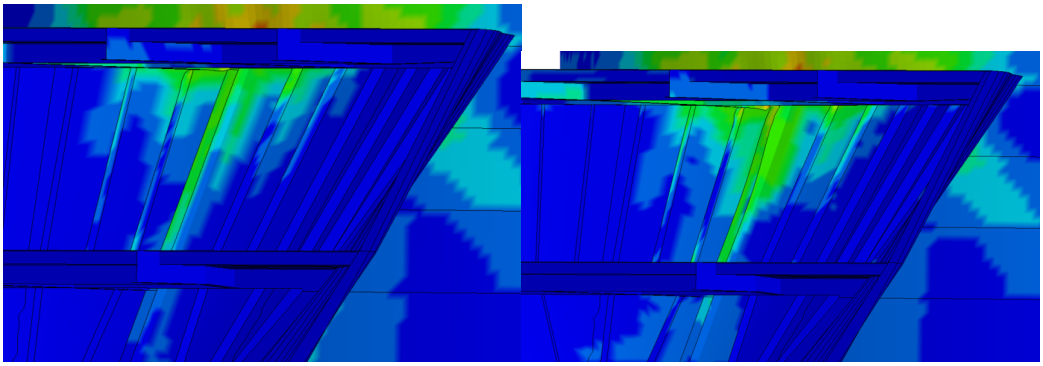

(a) Center plate at initial peak of force-deformation curve.

(b) Center plate right after initial peak of force-deformation curve.

Figure 8.6: Deformation of centerplate, plottet with the von Mises stress.

8.3 Shipside collision

In the case of the collision between the side of the vessel and the tower, the model used for the side is the one described in chapter 6.2.3. As for the tower model, the model described in chapter 6.1 is used, however, as the shipside model has a quite large height, increasing the collision area, the tower model had to be higher so that the boundary conditions at the top and bottom end did not intervene with the collision resistance in the models. Therefore the tower height was increased by 8 meters on both ends, giving a total of 32 meters. The collision model is shown in figure 8.7.

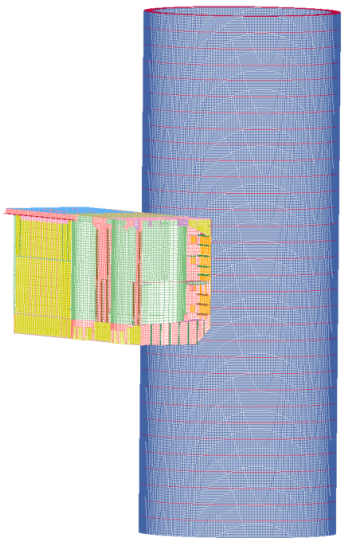

Figure 8.7: Model of collision between shipside and tower.

Figure 8.8 show the force-deformation curve for the side collision. As in the case of the bulb collision, it can be seen from the figure that the vessel will only have small deformations and that the tower will dissipate most of the energy. The vessel will only deform in the early phase of the collision, while the impact force is low, but the impact force will quickly rise to about 18 MN where the tower will start to have significant deformation. After this point the resistance in the tower will increase slowly, before flattening out around 23 MN.

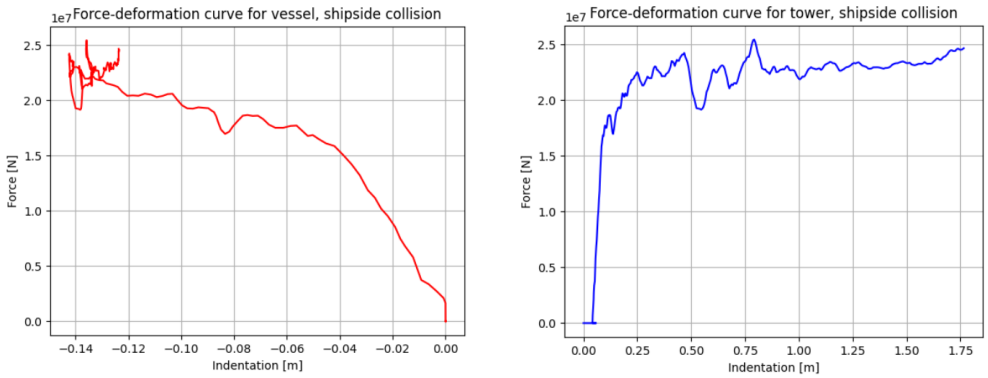

(a) Force-deformation curve for the vessel stern corner.

(b) Force-deformation curve for the tower section.

Figure 8.8: Force-deformation curves.

8.3.1 Discussion

From the recommended force-deformation relationship in figure 4.5 it is expected that the resistance in the broad side of the vessel is very high, as it increases quickly to at least 25 MN without significant deformation. This is reflected in the simulation as the vessel deforms slightly in the very early phase of the collision before the tower starts dissipating the collision energy. The tower, however, has a much higher resistance than what is expected from DNV's proposed resistance. One reason for this is that the model from DNV corresponds to an unstiffened tubular member while the tower in this case is ring-stiffened. This is accounted for by establishing an equivalent thickness for the tower, by taking the area of the stiffener, dividing it over the stiffener spacing, and adding it to the original thickness as shown in equation 8.1. The result with the equivalent thickness is shown in figure 8.9. The curve proposed by DNV is established using the relevant B/D relationship of 0.63. The value of k is set to 1 on suggestion from the supervisor. It can be seen that the curves are somewhat similar, as they both increase quickly for small deformations, before flattening out the larger the indentations becomes. The difference is that the resistance from the tower section increases much more in the initial phase, meaning that it is larger than what is expected from DNV's proposed models.

$$t = t_0 + \frac{A}{l} \tag{8.1}$$

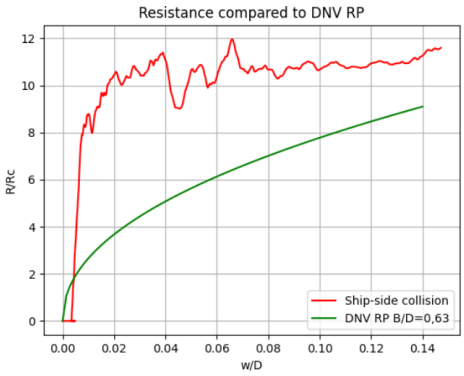

Figure 8.9: tower resistance compared to DNV RP.

One thing to notice when looking at the resistance is that the curve proposed by DNV is quite similar to the resistance in the tower for the bulb collision. This may be due to the fact that in both cases the vessel will dissipate very little energy, meaning that the tower will have major deformations. The main difference in these simulations, however, is the shape of the part of the vessel that collides with the tower. In the case of the shipside collision, the collision area will be much larger and the collision energy will be distributed more evenly, while for the bulb, which has a rounder and smaller collision area, the impact force will be more concentrated in local areas. This means that it is as expected that the tower can better resist deformations in the collision with the shipside. Figure 8.10 shows the resistance for both bulb and side collision, compared to proposed models. It shows that the overall highest compliancy is between the bulb collision and the relevant curve from DNV. In this case, the curve overestimates the resistance in the tower, which could be due to the different shapes that the collision area has. For the side collision, which is what DNV's proposed model is applied for, the resistance is as mentioned underestimated. This is also the case for the proposed models in the report from Ícaro Ladeira from Nantes University. This model, however, has limitations regarding the fact that the length of the tubular member is highly relevant, and needs to be larger than 9 times the diameter. In this case, the yield stress is set to the value for the tower material, and the length is 108 m, which is 9 times the diameter. It also does not become completely dimensionless when dividing it by the characteristic denting resistance R_c, since the thickness in this equation is exhalted in 1.22. In addition, it is linearly dependent on the degree of indentation, which for both the simulation and the proposed model from DNV is not the case.

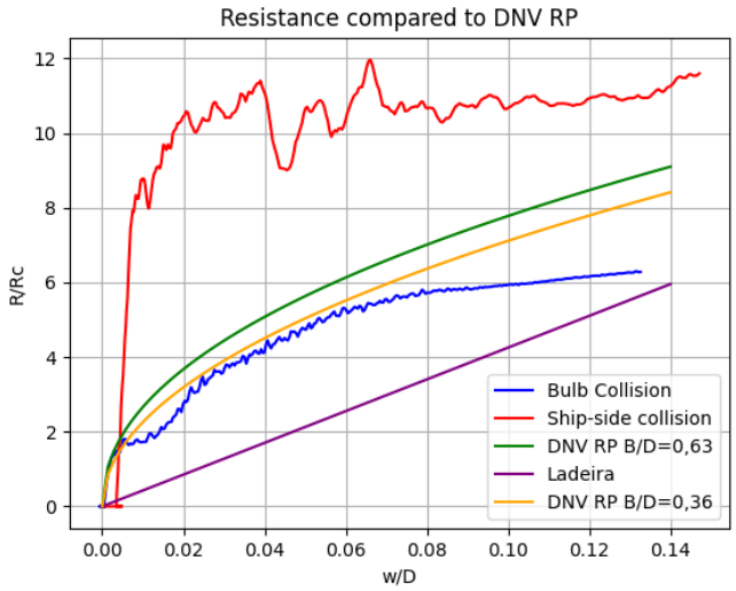

Figure 8.10: Resistance in the tower compared to analytical models.

8.4 Stern corner collision

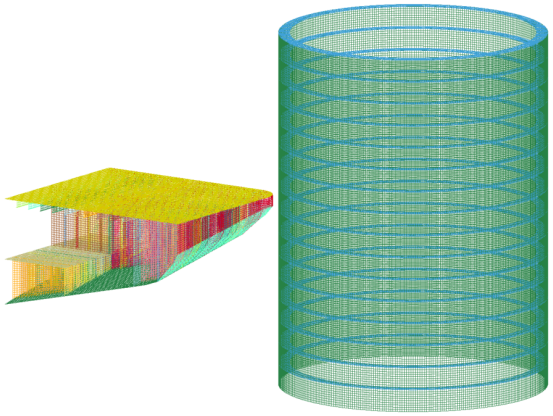

Figure 8.11: Stern corner collision model.

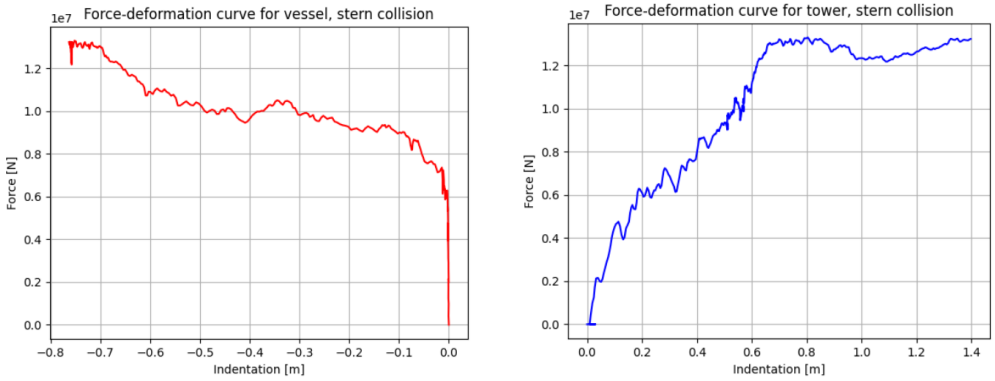

(a) Force-deformation curve for the vessel stern corner.

(b) Force-deformation curve for the tower section.

Figure 8.12: Force-deformation curves.

In the collision simulation between the tower and the stern corner, the model described in chapter 6.2.2 is used, along with the same tower model as the previous collision simulations. The models are shown in figure 8.11. The force-deformation curves are plotted in figure 8.12. As for the forecastle collision, in the collision between the tower and the stern corner of the vessel, the tower dissipates most of the energy in the initial phase. The vessel does not deform by a significant amount until the collision force reaches 6 MN, where both the tower and vessel will deform and share the dissipation of the energy. In the phase where the collision force is between 6 MN and about 13 MN, the vessel will deform by about 0.8 meters, while the tower deforms by almost 0.6 meters, showing that in this phase they both dissipate energy. However, in the last phase, the resistance of the vessel has increased and it does not deform further. This is not the case for the vessel, as the indent still increases up to almost 1.4 meters.

8.4.1 Discussion

Comparing the force-deformation curves for stern corner collision in figure 8.12 with the recommended force-deformation curves from DNV in figure 4.5 shows that the results agree quite well. The recommended curves concern vessels between 6500 and 10000 tons colliding with a tower with a diameter above 10 m such as in this case. Both curves rise quickly in the initial part of the collision, for small indentations, before the increase rate steadily decreases up to 0.75 meters indentation, where the impact force has risen to about 12-14 MN. This is where the tower

starts dissipating most of the energy in the LS-DYNA simulation. In the recommendation from DNV the analysis is done with a rigid tower, meaning that the impact force and indentation in the vessel continue to increase.

8.5 Hourglass energy

Hourglass modes are nonphysical zero-energy deformation modes that arise in under-integrated elements, that produce no stress and no strain (LS-DYNA-Support 2023a). While fully integrated solids and shells do not hourglass, they are much more expensive and time-consuming, and may also be less robust for large deformations. Some of the hourglass modes tend to oscillate with shorter periods than the periods of the structural response. One possibility for resisting the undesirable hourglass modes is with a viscous damping or small elastic stiffness that is capable of stopping the formation of anomalous modes but has negligible effects regarding the stable global modes (LS-DYNA 2022).

For solids, the 12 hourglass-resisting force vectors are

$$f_{i\alpha}^{k} = a_h h_{i\alpha} \Gamma_{\alpha k} \tag{8.2}$$

where

$$h_{i\alpha} = \sum_{k=1}^{8} \dot{x}_i^k \Gamma_{\alpha k} \tag{8.3}$$

which is zero if the element velocity field has no hourglass component, and nonzero if the modes are present. The hourglass modes for solids and shells are presented in figures 8.13 and 8.14 respectively. $\Gamma_{\alpha k}$ is the hourglass base vectors presented in table 8.1 and

$$a_h = Q_{\mathrm{HG}} \rho v_{\mathrm{e}}^{2/3} \frac{c}{4} \tag{8.4}$$

where v_{e} is the element volume, c is the material sound speed and Q_{HG} is a constant usually set between 0.05 and 0.15.

	$\alpha = 1$	$\alpha = 2$	$\alpha = 3$	$\alpha = 4$
Γ_{j1}	1	1	1	1
Γ_{j2}	1	-1	-1	-1
Γ_{j3}	-1	-1	1	1
Γ_{j4}	-1	1	-1	-1
Γ_{j5}	-1	-1	1	-1
Γ_{j6}	-1	1	-1	1
Γ_{j7}	1	1	1	-1
Γ_{j8}	1	-1	-1	1

Table 8.1: Hourglass base vectors

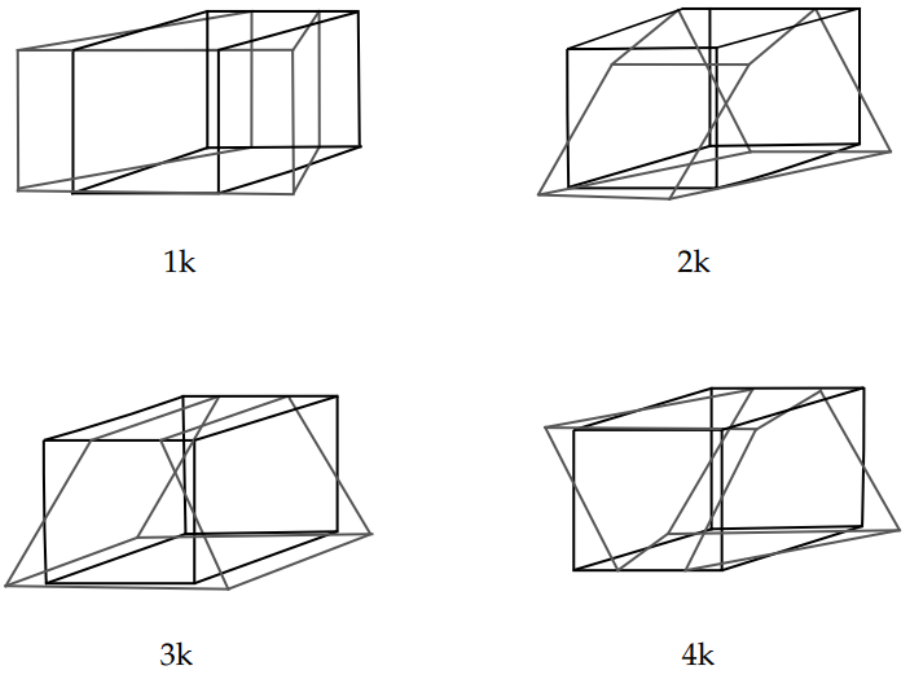

Figure 8.13: Hourglass modes of an eight-node element with one integration point (LSTC 2012).

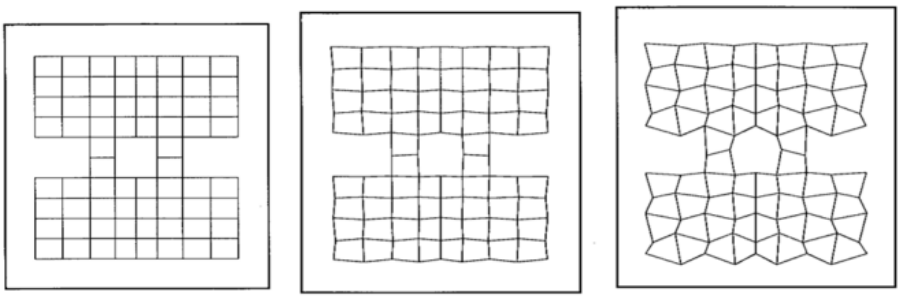

(a) Case 1: No hourglassing evident. (b) Case 2: Moderate to severe hourglassing. (c) Case 2 with displacements scaled up.

Figure 8.14: Hourglass modes in shells (LSTC 2012).

One limitation of this hourglass control type is that the resisting forces are not orthogonal to the linear velocity field when elements are not parallelepipeds, meaning they can still generate hourglass energy. Flanagan and Belytschko developed an hourglass control that is orthogonal to all modes that are not zero energy hourglass modes by defining the hourglass velocity field to resist components of the velocity field that are not part of the fully linear field. The velocity field is defined as

$$\dot{x}_i^{k\mathrm{HG}} = \dot{x}_i^k - \dot{x}_i^{k\mathrm{LIN}} \tag{8.5}$$

where

$$\dot{x}_i^{k\mathrm{LIN}} = \dot{\bar{x}}_\mathrm{i} + \dot{\bar{x}}_{i,j}\left(x_j^k - \bar{x}_j\right) \tag{8.6}$$

and

$$\begin{aligned} \bar{x}_i &= \frac{1}{8}\sum_{k=1}^{8} x_i^k \\ \dot{\bar{x}}_i &= \frac{1}{8}\sum_{k=1}^{8} \dot{x}_i^k \end{aligned} \tag{8.7}$$

The shape vectors are orthogonal to the fully linear velocity field and the rigid

body field and can resist the hourglass velocity deformations. The hourglass shape vectors then become

$$\gamma_{\alpha k} = \Gamma_{\alpha k} - \phi_{k,i} \sum_{n=1}^{8} x_i^n \Gamma_{\alpha n} \tag{8.8}$$

and equations 8.3 and 8.2 become

$$g_{i\alpha} = \sum_{k=1}^{8} \dot{x}_i^k \gamma_{\alpha k} = 0 \tag{8.9}$$

and

$$f_{i\alpha}^k = a_h g_{i\alpha} \gamma_{\alpha k} \tag{8.10}$$

The hourglass control type used in these analyses is type 4, which is similar to the Flanagan Belytschko type described, except that it evaluates the hourglass stiffness rather than viscosity. This means that the hourglass forces are proportional to the total hourglass deformation, rather than hourglass velocity, allowing the elements to spring back and absorb less energy than for the viscous control types. Stiffness types of control are preferred for crash simulations, but may also artificially stiffen the response, meaning that the hourglass coefficient should be reduced (LSTC 2012). Therefore, the hourglass coefficient in the analyses was set to 0.03.

8.5.1 Hourglass energy results

The rule of thumb regarding hourglass energy is that it should not exceed 10% of the internal energy. The hourglass energy divided by the internal energy is therefore presented in figures 8.15 and 8.16 to assess the effect on the simulations.

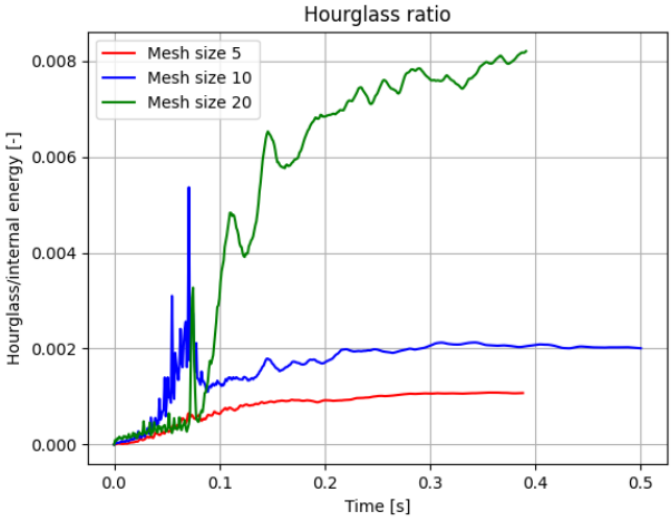

Figure 8.15: Hourglass energy divided by internal energy for the mesh convergence analyses.

As shown in figure 8.15, the hourglass energy is not even close to the limit of 10% of the internal energy as it only reaches about 0.8% at the most. This is for the largest mesh size, which is logical, as one way of minimizing the hourglass energy is by refining the mesh. Apart from a large peak for the 10 cm mesh size analysis, this is shown by the figure as well, as the energy ratio only is smaller for the smaller meshes. As for the side, stern corner, and forecastle simulations, figure 8.16 shows that the ratio between hourglass and internal energy is higher, peaking at about 1.5 % for the forecastle simulation, which is still very much within the accepted range.

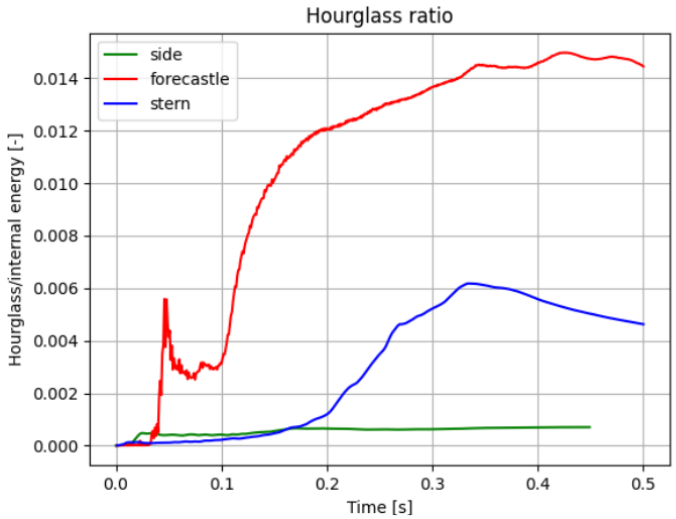

Figure 8.16: Hourglass energy divided by internal energy for the side, stern corner and forecastle collisions.

Figures 8.15 and 8.16 show the ratio of the hourglass energy and the internal energy for the system. However, this needs to be checked for individual parts as well. For the bulb collision, the parts with the highest values of hourglass energy are in the stiffeners and walls of the tower. These are presented in Section B. This is also done for the other simulations, and presented in the same chapter. The hourglass energy rarely approaches 5 % of the internal energy.

Chapter 9

Residual strength analyses

Figure 9.1: Tower with rotational motion creating bending moment.

The residual strength analysis is performed in order to assess the integrity of the damaged tubular. This is done by applying a rotating motion to the top of the already damaged cylinder, creating an increasing bending moment. The rotation is set so that the damaged part of the tubular is put under compression, while the other side is under tension. The motion rotates around a point in the center of the top end of the tower, which is shown in figure 9.1. The damaged tower section is shown in figure 9.2 both before and after it was subjected to an increasing bending moment.

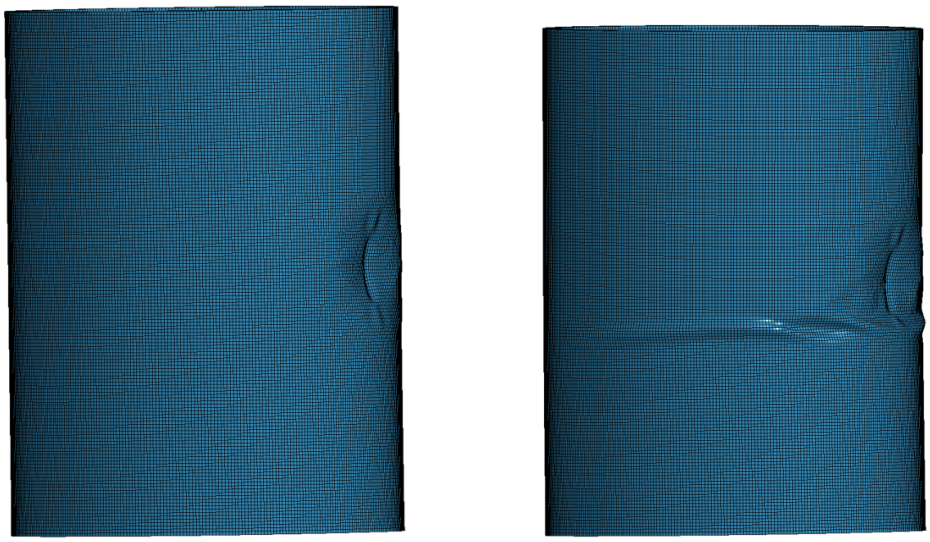

(a) Tower section before bending moment. (b) Tower section after bending moment.

Figure 9.2: Damaged tower section subjected to bending moment.

9.1 Bulb collision

The results from the residual strength assessment of the tower damaged by the bulb collision are shown in figure 9.3. As expected, the bending moment capacity of the tower decreases as the magnitude of the indentation increases. From the theory discussed in chapter 4.7.3, it is also expected that the decrease in bending moment capacity is not linear, but instead that just small initial imperfections to the cylinder decrease the capacity significantly, and that increasing the degree of indentation further will have less and less effect on the bending moment capacity. This is for example shown in figure 9.3, where a 15 cm indent decreases the moment capacity of the tower from over 0.9 GNm, to just under 0.7 GNm, while a further 15 cm indent only decreases the capacity by under 0.1 GNm.

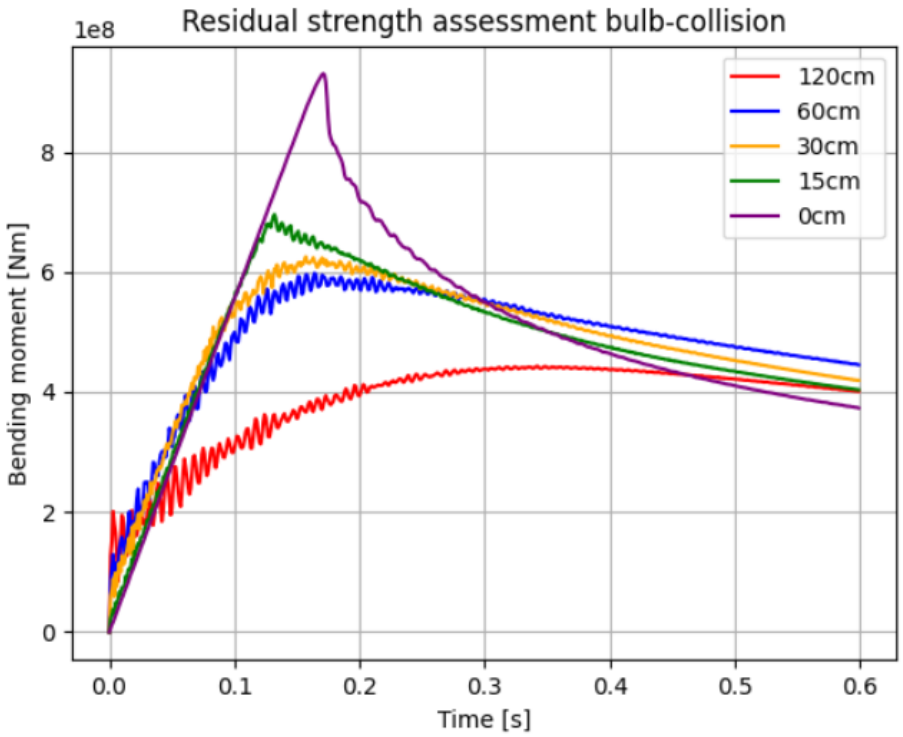

Figure 9.3: Residual strength assessment for bulb collision.

9.2 Side collision

Figure 9.4 shows the residual strength of the tower subjected to shipside collision. It shows that the decrease in strength is much larger for the tower subjected to side collision compared to the tower subjected to bulb collision, as the moment capacity drops from around 0.9 GNm to just below 0.5 GNm for an indent of 30 cm. Increasing the indent to 60 cm does, however, not decrease the capacity very much, as it stays between 0.4 and 0.45 GNm.

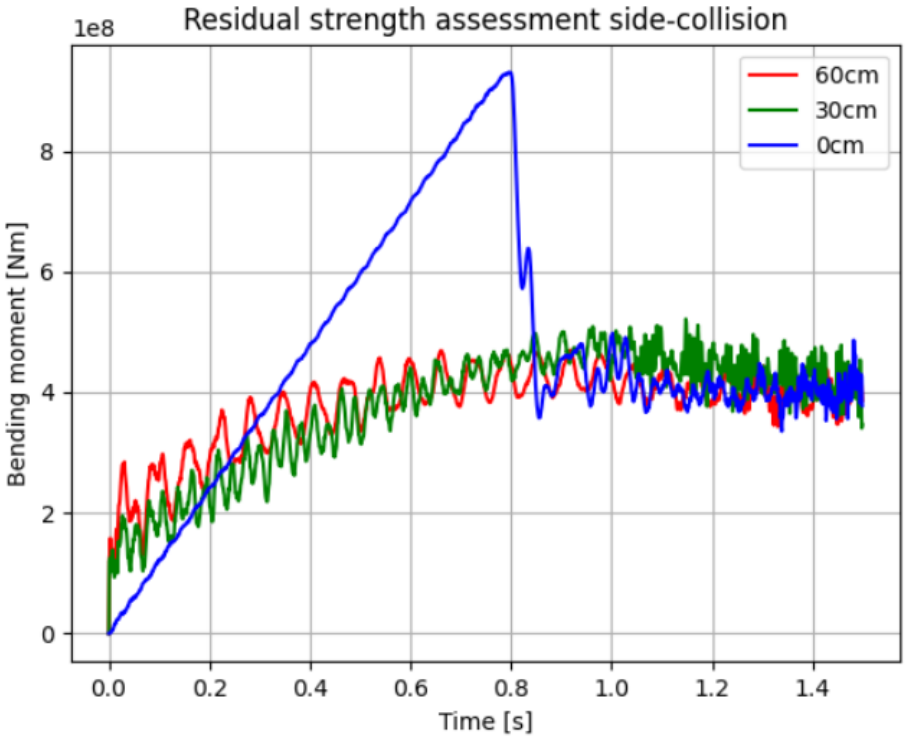

Figure 9.4: Residual strength assessment for side collision.

9.3 Discussion

Table 9.1 and figure 9.5 show the capacity and reduction of the bending moment of the tower, for different degrees of indentation. It compares the reduction proposed in DNV RP with the results obtained in this investigation. The results show that the proposed model from DNV underestimates the effect of indentations compared to the results from the analysis. Both the tower subjected to bulb collision and the tower subjected to side collision will experience a significantly larger reduction in moment capacity than what is expected. The reason for this may be due to the large diameter and small thickness, and that the tower is ring stiffened. However, table 9.1 shows that even at full strength, the moment capacity of the tower is lower than expected.

Small inaccuracies may occur in these analyses though, due to the fact that the bending moment varies, and no absolute certain point is easily read as the max-

imum capacity for most cases. The trend, however, stays the same that the capacity in this analysis is much more affected by indentation than what is proposed in DNV RP C204. The oscillations in the bending moment that can be seen in the figures could be due to dynamic effects in the tower. To reduce these dynamic effects, the rotational motion in the top end of the tower, creating the bending moment, is set to be slow. However, there may still be some inaccuracies due to these effects.

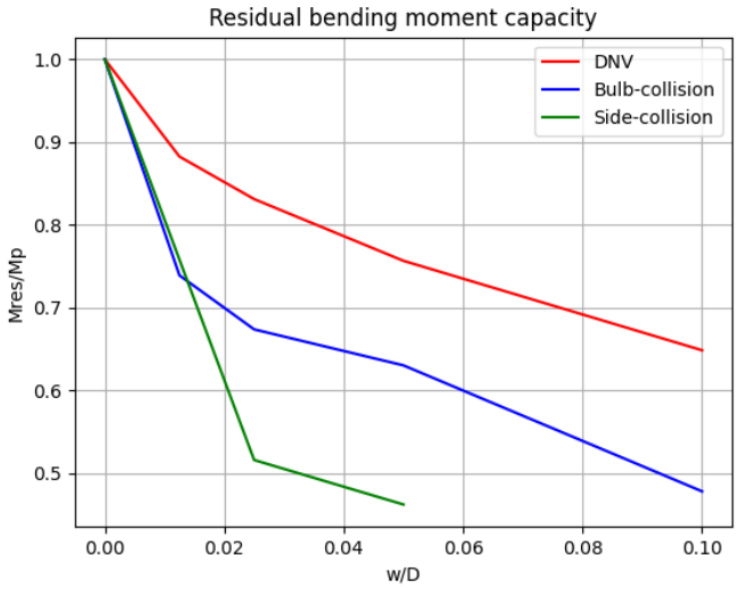

Figure 9.5: Reduction of moment capacity due to local dents.

w/D	**Bulb [GNm]**	M_p/M_{res}	**Side [GNm]**	M_p/M_{res}	**DNV RP [GNm]**
0	0.92	1	0.93	1	1.22
0.0125	0.68	0.74			1.07
0.025	0.62	0.67	0.48	0.52	1.01
0.05	0.58	0.63	0.43	0.46	0.92
0.1	0.44	0.48			0.79

Table 9.1: Bending moment capacity of the tower for bulb and side collision, compared to DNV RP.

According to the report "A review of structural responses and design of offshore tubular structures subjected to ship impacts" (Yu and Amdahl 2018) the model

from DNV is conservative compared to other proposed models because there is no contribution from the dented part. This means that the results obtained from the simulations show that the tower is even more sensitive to indentations compared to the other models. These other models are compared in figure 9.6.

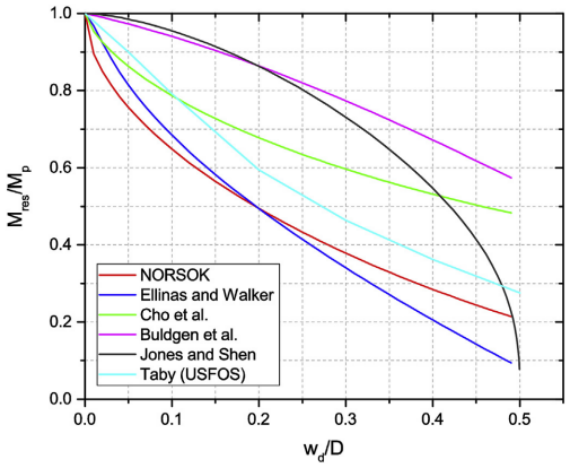

Figure 9.6: Comparison of models proposed for residual strength assessments (Yu and Amdahl 2018).

9.4 Assessment of acceptable damage levels

To evaluate whether the damage to the tower has to be considered critical it has to be compared to the buckling criteria. This is described in chapter 4.2. The expected applied loads can be taken from the 15 MW reference turbine, where it can be seen from figure 9.7 that at rated wind speed of 10.59 m/s the thrust force in the rotor is almost 3 MN. Multiplying this with the rotor height of 150 m gives a total bending moment of 0.45 GNm. Using the safety factors described in chapter 4.2 then gives a required bending moment capacity of 0.675 GNm. From the analysis of the bulb collision, it can be seen that both the case where the tower is undamaged and the case where the indentation is 15 cm will satisfy this requirement. However, for the side collision, only the undamaged tower will satisfy this requirement. This could again be due to the large collision area where the strength of the tower is compromised. For the side collision, the 15 cm indentation simulation has not been run and if the curve for the reduction of bending moment capacity in figure 9.5 is accurate, the tower subjected to shipside collision could also possibly satisfy the buckling criteria.

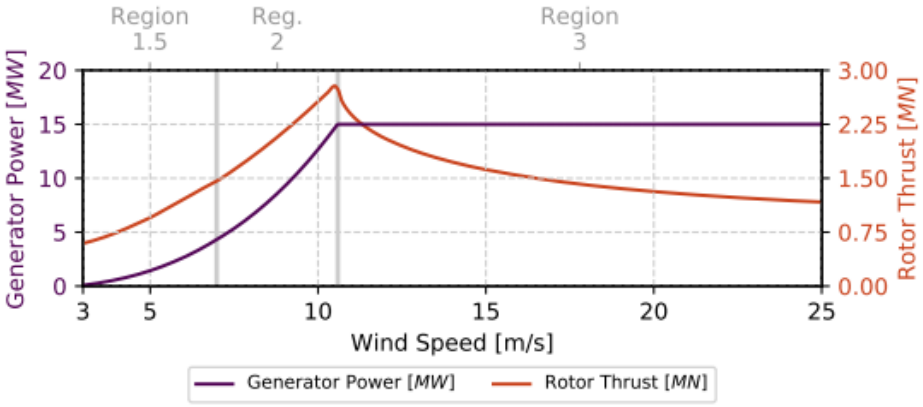

Figure 9.7: Rotor thrust in the 15 MW reference turbine (NREL 2020).

Chapter 10

Discussion and conclusion

Offshore wind energy has great potential for producing energy with limited environmental damage. Improved wind conditions, higher possibility for scale-ups, and less pollution are just some of the advantages of offshore wind. In addition, floating substructures eliminate some of the challenges of offshore wind compared to bottom fixed structures, such as water depth.

However, this could mean higher needs for maintenance and service of the turbines, in addition to the farms being located closer to ship traffic lanes. Along with more hostile conditions around the wind farms, this could increase the risk of ships colliding with the turbines. The consequences range from minor structural damages to the collapse of the turbines. Generally, much of the focus on assessing these collisions has been put on accidental events with a low probability of occurrence. Therefore, assessing collisions with a higher probability of occurrence is also necessary.

In this thesis, collisions between the tower of a floating offshore wind turbine and supply vessels have been investigated and analyzed. The main focus has been on the denting and residual strength of the tower, but also the response of the vessel has been investigated. The non-linear FEM software LS-DYNA has been used to perform simulations of a tower model colliding with the model of a typical modern supply vessel with a displacement of 7500 tons.

Analytical models of the denting resistance and residual strength of a tubular member subjected to ship collision have been investigated and compared to the results of this analysis. The force-deformation curves established from the sim-

ulation agree quite well with what is expected from recommended results, especially for the vessels. Regarding the denting resistance of tubular members, the analytical models proposed in DNV's recommended practices and the report from Nantes University both underestimate the resistance compared to the results from this analysis. This can have several causes, for example, significant changes have happened both to wind turbines and vessels since some of the models were established. In addition, this analysis does not account for the global motions of either the vessel or the tower, and the speed is at a constant 5 m/s. This is not the case in reality as some of the energy would be dissipated from the motions of the structures, and the speed of the vessel would be affected by the impact.

The residual strength of the turbine tower has also been assessed to investigate the effects indentations have on the moment capacity and the effect it has on the tower's ability to comply with regulations. The results show that only small indentations in the tower will decrease the bending moment capacity of the tower significantly. Compared to proposed models for assessing the moment capacity reduction, the tower in this analysis will have a much larger effect of indentation. Even a small indentation of 0.05 of the diameter can decrease the capacity by almost 50% in the case of the shipside collision. This decrease is not as substantial for the bulb collision, but it is still larger than what is expected from investigated models.

Regulations regarding acceptable damage levels and relevant safety factors from Bureau Veritas' NI572 along with the residual strength of the tower imply that, in the case of the 15 MW reference turbine, indentations over 15 cm (0.0125 of the diameter) would decrease the moment capacity of the tower enough that it can not comply with the ULS criteria.

Ultimately, the final results from the analyses in this thesis imply several things. Firstly, the recommended force-deformation curves for ship impact used in DNV recommended practices have a high degree of accuracy, as they agree quite well with what is suggested by the impact simulations in this thesis. Secondly, new analytical models for the resistance to indentation of tubular members may need to be established, or existing models may need to be modified, as the existing models significantly underestimate the resistance in the tower compared to what is seen in the simulations. Ultimately, proposed models for assessing the residual strength of dented tubulars may also need to be modified, or new ones established. The effect of indentations in the tower is considerably higher than what is proposed, and only small imperfections could lead to the tower not having sufficient residual strength to comply with criteria from classification societies. However, the analyses in this thesis are not viewed as deep and comprehensive enough to establish new models,

or propose changes to the existing models, but rather serve as an evaluation of the models.

Chapter 11

Further work

Further work from this thesis could include more comprehensive analyses both on the collisions and the residual strength. The collision analyses could include different collision scenarios, such as different collision speeds and impact angles. In addition, to assess the analytical models for denting resistance, different characteristics of the tower could be analyzed, such as different thicknesses or diameters. Also, collisions with various other components of wind turbine structures may be assessed, such as columns, braces, or joints.

Regarding residual strength, simulations with a higher number of degrees of indentations could make the results more accurate. Also, in this thesis, only the bending moment capacity has been evaluated, and effects of additional axial compressive forces have not been taken into account. Similar to denting resistance assessment, the main characteristics of the tower have an effect on the residual strength, and more detailed analyses of this could improve the overall understanding of the residual strength.

References

Amdahl, Jørgen (2005). 'Buckling of Cylindrical Shells'. Chapter.

Amdahl, Jørgen and Zhaolong Yu (2018). *Analysis and design of offshore tubular members against ship impacts*. NTNU.

— (n.d.). 'Design against ship collisions in accordance with the new DNV RP-C204'. Powerpoint.

Andersen, Ina (2022). 'Nytt havvindsamarbeid: Melder seg på i kampen om flytende havvind på Utsira Nord'. In: *Teknisk Ukeblad*. URL: https://www.tu.no/artikler/nytt-havvindsamarbeid-melder-seg-pa-i-kampen-om-flytende-havvind-pa-utsira-nord/523587?key=9lUe7qnK.

Andersen, Margrethe (2022). 'DNV awards Odfjell Oceanwind AiP for new Deepsea Semi™ floating offshore wind foundation'. In: *DNV*. URL: https://www.dnv.com/news/dnv-awards-odfjell-oceanwind-aip-for-new-deepsea-semi-floating-offshore-wind-foundation-219132.

Commission, European (2019). *2030 climate energy framework*. URL: https://climate.ec.europa.eu/eu-action/climate-strategies-targets/2030-climate-energy-framework_en (visited on 12th Dec. 2022).

— (2020). *An EU Strategy to harness the potential of offshore renewable energy for a climate neutral future*. European Commission.

— (2022). *REPowerEU Plan*. European Commission.

Dai, Lijuan et al. (2013). 'Risk of collision between service vessels and offshore wind turbines'. In: *Reliability Engineering System Safety* 109, pp. 18–31. ISSN: 0951-8320. DOI: https://doi.org/10.1016/j.ress.2012.07.008. URL: https://www.sciencedirect.com/science/article/pii/S0951832012001585.

DNV (2021a). *DNV-RP-C204 Structural design against accidental loads*. DNV.

— (2021b). *DNV-ST-0119 Floating wind turbine structures*. DNV.

Du, Aaron Zigeng and Eric Paya (2020). *Floating Offshore Wind is Here to Stay*. Empire Engineering. URL: https://www.empireengineering.co.uk/floating-offshore-wind-is-here-to-stay/ (visited on 12th Sept. 2022).

LS-DYNA (July 2017). *LS-DYNA® KEYWORD USER'S MANUAL VOLUME II*. English. Version R10. LS-DYNA. 1543 pp. July 26, 2017.

— (Aug. 2022). *LS-DYNA® Theory Manual*. English. LS-DYNA. 1543 pp. August 06, 2022.

LS-DYNA-Support (2023a). *Hourglass*. URL: https://www.dynasupport.com/howtos/element/hourglass (visited on 4th Aug. 2023).

— (2023b). *Time Integration*. URL: https://www.dynasupport.com/tutorial/ls-dyna-users-guide/time-integration (visited on 3rd Jan. 2023).

EESI (2016). *Offshore Wind: Can the United States Catch up with Europe?* Environmental and Energy Study Institute.

Energydata.info (2023). *Global Wind Atlas*. URL: https://globalwindatlas.info/en/ (visited on 6th Aug. 2023).

Equinor (2019). *PUD del II - Konsekvensutredning*. Equinor.

— (2023). *First power from Hywind Tampen*. URL: https://www.equinor.com/news/20221114-first-power-from-hywind-tampen.

— (2022). *Hywind Tampen*. URL: https://www.equinor.com/energy/hywind-tampen (visited on 10th Dec. 2022).

Fimreite, Stina Bjørgo (2022). *Fluid Structure Interaction Analysis of Abnormal Wave Slamming Events*. XXX.

Gaertner, Evan et al. (2020). *Definition of the IEA 15-Megawatt Offshore Reference Wind*. National Renewable Energy Laboratory.

Hansen, Anne Marit (2018). 'Havvind og marint liv - dialogmøte'. Presentation.

Hockenos, Paul (2020). 'Will Floating Turbines Usher in a New Wave of Offshore Wind?' In: *Yale Environment 360*. URL: https://e360.yale.edu/features/will-floating-turbines-usher-in-a-new-wave-of-offshore-wind.

Hong, Lin (2009). 'Simplified Analysis and Design of Ships subjected to Collision and Grounding'. PhD thesis. NTNU.

Hopstad, Anne Lene Haukanes, Knut Olav Ronold and Johan Slätte (2013). 'Design Standard for Floating Wind Turbine Structures'. Deepwind 2013. URL: https://www.sintef.no/globalassets/project/deepwind-2013/deepwind-presentations-2013/posters/hopstad_poster.pdf.

IEA (2019). *Offshore WindOutlook 2019*. IEA.

Jørgen Amdahl, Tore Holmås (2011). *HIGH ENERGY SHIP COLLISIONS WITH JACKET SUPPORTED OFFSHORE WIND TURBINES*. Marine 2011 conference.

Collisions Between Platforms and Ships in Norway in the Period 2001-2010 (June 2011). Vol. Volume 2: Structures, Safety and Reliability. International Conference on Offshore Mechanics and Arctic Engineering, pp. 637–641.

Ladeira, Ícaro (2022). *THE STRUCTURAL RESPONSE OF OFFSHORE WIND TURBINES SUBJECTED TO LOW-ENERGY SHIP IMPACTS*. Icam Nantes.

Liu, Zhenhui and Jørgen Amdahl (2019). 'On multi-planar impact mechanics in ship collisions'. In: *Marine Structures* 63, pp. 364–383. ISSN: 0951-8339. DOI: https://doi.org/10.1016/j.marstruc.2018.10.006. URL: https://www.sciencedirect.com/science/article/pii/S0951833918300947.

LSTC (2012). 'Hourglass'. Presentation. URL: https://ftp.lstc.com/anonymous/outgoing/jday/hourglass.pdf.

NREL (2020). *New Reference Turbine Gives Offshore Wind an Upward Draft*. URL: https://www.nrel.gov/news/program/2020/reference-turbine-gives-offshore-wind-updraft.html (visited on 10th Dec. 2022).

Ørsted (2019). *Making green energy affordable*. URL: https://orsted.com/en/insights/white-papers/making-green-energy-affordable/1991-to-2001-the-first-offshore-wind-farms (visited on 9th Sept. 2022).

Presencia, Carla E. and Mahmood Shafiee (2018). 'Risk analysis of maintenance ship collisions with offshore wind turbines'. In: *International Journal of Sustainable Energy* 37.6, pp. 576–596. DOI: 10.1080/14786451.2017.1327437. URL: https://doi.org/10.1080/14786451.2017.1327437.

Ren, Yongli et al. (2022). 'Dynamic behavior and damage analysis of a spar-type floating offshore wind turbine under ship collision'. In: *Engineering Structures* 272, p. 114815. ISSN: 0141-0296. DOI: https://doi.org/10.1016/j.engstruct.2022.114815. URL: https://www.sciencedirect.com/science/article/pii/S0141029622008999.

Skallerud, Bjørn and Jørgen Amdahl (2002). *Nonlinear Analysis of Offshore Structures (Civil and Structural Engineering Series)*. Research Studies Press, pp. 169–190.

Terndrup Pedersen, P. and Shengming Zhang (1998). 'On Impact mechanics in ship collisions'. In: *Marine Structures* 11.10, pp. 429–449. ISSN: 0951-8339. DOI: https://doi.org/10.1016/S0951-8339(99)00002-7. URL: https://www.sciencedirect.com/science/article/pii/S0951833999000027.

Tong, K.C (1998). 'Technical and economic aspects of a floating offshore wind farm'. In: *Journal of Wind Engineering and Industrial Aerodynamics* 74-76, pp. 399–410. ISSN: 0167-6105. DOI: https://doi.org/10.1016/S0167-6105(98)00036-1. URL: https://www.sciencedirect.com/science/article/pii/S0167610598000361.

UN (2021). *Decision -/CP.26 Glasgow Climate Pact*. UN.

Vanelli, T., J. Rinker and D. S. Zalkind (2022). *Aeroservoelastic stability of a floating wind turbine*. National Renewable Energy Laboratory.

Veritas, Bureau (2019). *Classification and Certification of Floating Offshore Wind Turbines*. Bureau Veritas.

Vestas (2021). *V236-15.0MW*. Vestas.

WindEurope (2017). *Floating Offshore Wind Vision Statement*. WindEurope.
— (2022). *MThe US is about to build lots of offshore wind – what can it learn from Europe?* URL: https://windeurope.org/newsroom/news/the-us-is-about-to-build-lots-of-offshore-wind-what-can-it-learn-from-europe/ (visited on 12th Sept. 2022).
— (2023). *Offshore wind in Europe - key trends and statistics 2022*. WindEurope.
Simplified Analysis Tool For Ship-Ship Collision (July 2007). Vol. All Days. International Ocean and Polar Engineering Conference. eprint: https://onepetro.org/ISOPEIOPEC/proceedings-pdf/ISOPE07/All-ISOPE07/ISOPE-I-07-558/1809928/isope-i-07-558.pdf.
Yu, Zhaolong and Jørgen Amdahl (2018). 'A review of structural responses and design of offshore tubular structures subjected to ship impacts'. In: *Ocean Engineering* 154, pp. 177–203. ISSN: 0029-8018. DOI: https://doi.org/10.1016/j.oceaneng.2018.02.009. URL: https://www.sciencedirect.com/science/article/pii/S0029801818301495.
Yu, Zhaolong, Jørgen Amdahl et al. (2022). 'Numerical modelling and dynamic response analysis of a 10 MW semi-submersible floating offshore wind turbine subjected to ship collision loads'. In: *Renewable Energy* 184, pp. 677–699. ISSN: 0960-1481. DOI: https://doi.org/10.1016/j.renene.2021.12.002. URL: https://www.sciencedirect.com/science/article/pii/S0960148121017213.

Appendices

A Vessel/tower deformation

A.1 Bulb deformation

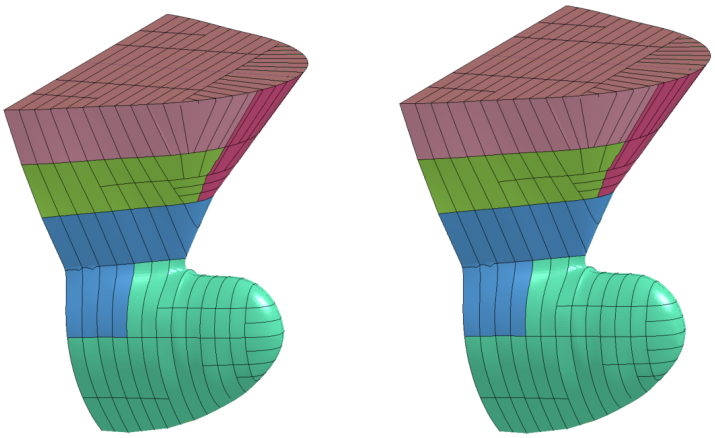

(a) Undeformed bulb. (b) Deformed bulb.

Figure A.1.1: Deformation of bulb.

B Hourglass and internal energy

B.1 Bulb collision

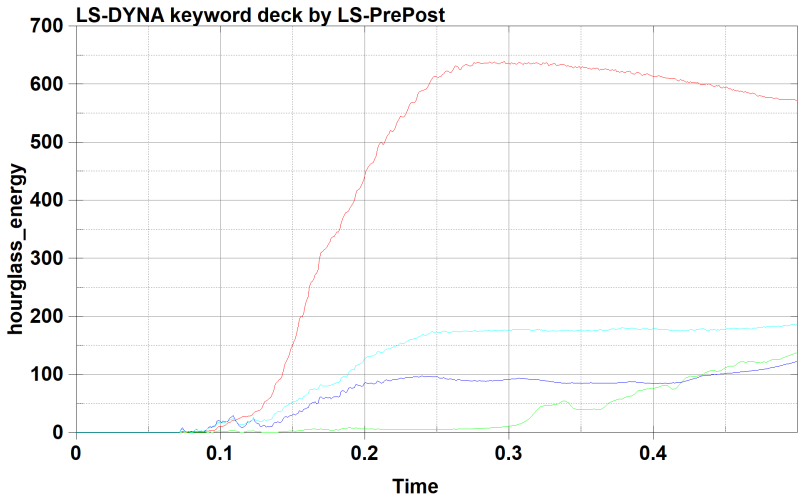

Figure B.1.1: Hourglass energy for higher-energy parts.

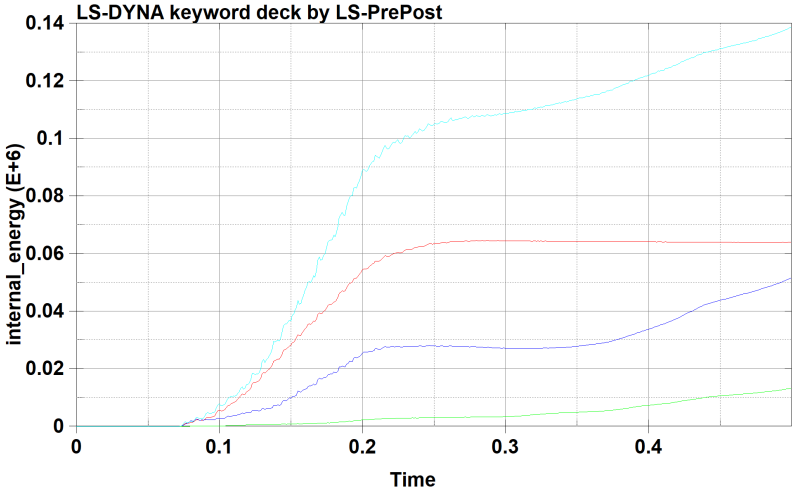

Figure B.1.2: Internal energy for higher-energy parts.

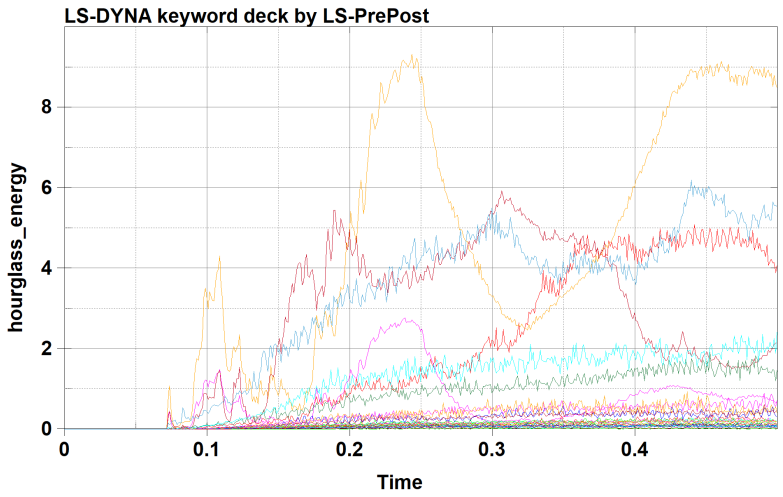

Figure B.1.3: Hourglass energy for low-energy parts.

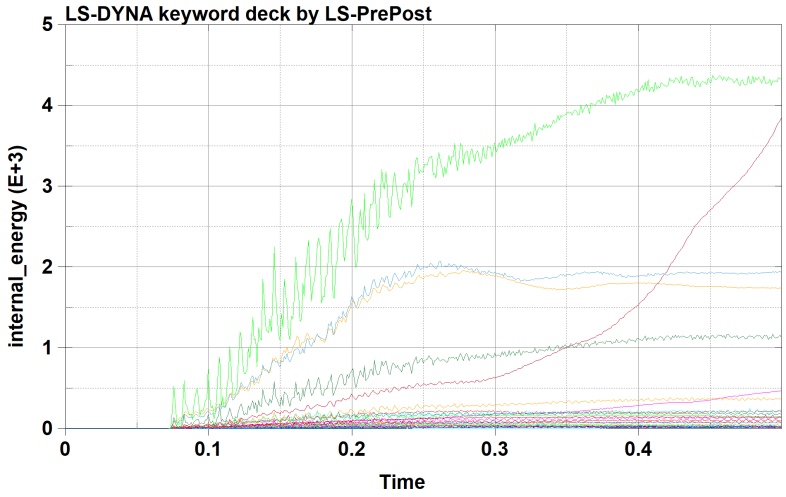

Figure B.1.4: Internal energy for low-energy parts.

B.2 Forecastle collision

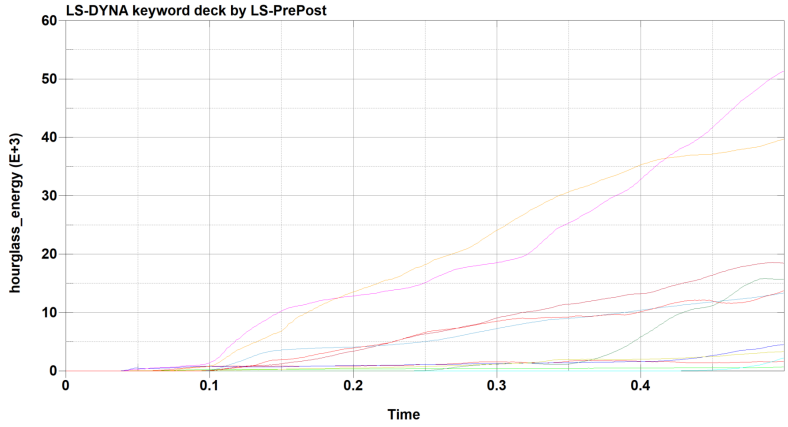

Figure B.2.1: Hourglass energy for high-energy parts.

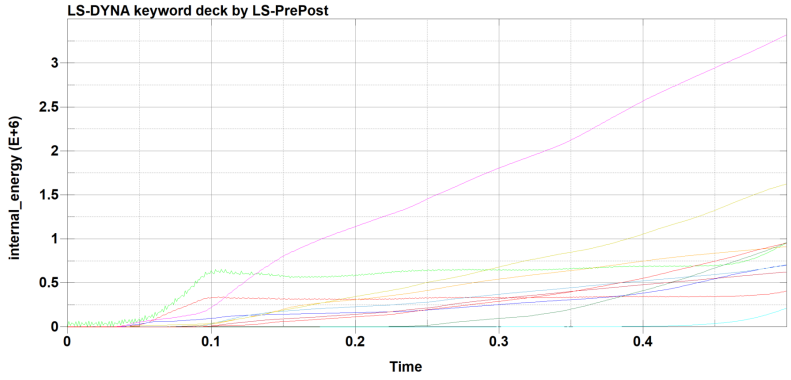

Figure B.2.2: Internal energy for high-energy parts.

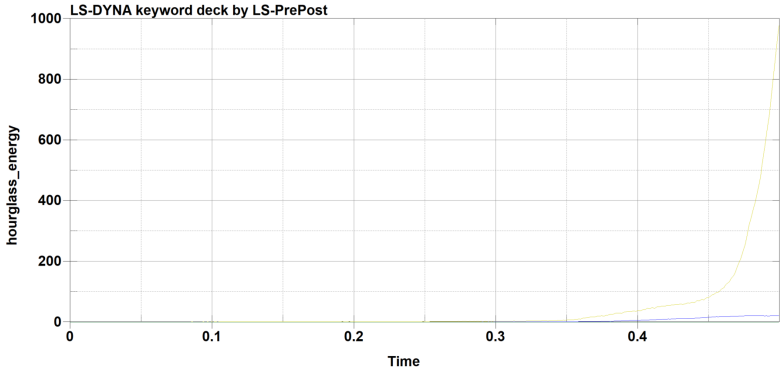

Figure B.2.3: Hourglass energy for medium-energy parts.

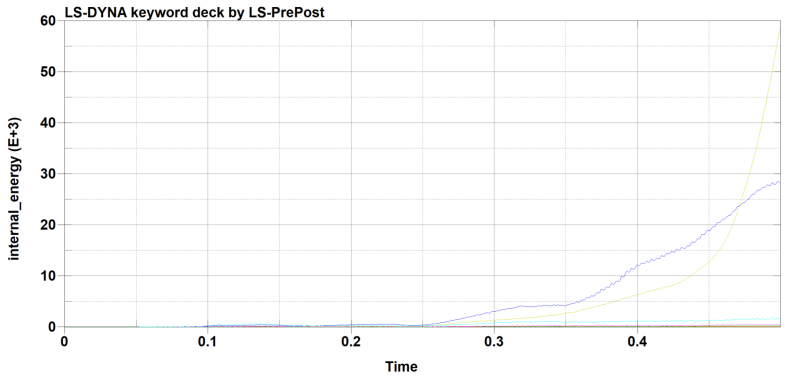

Figure B.2.4: Internal energy for medium-energy parts.

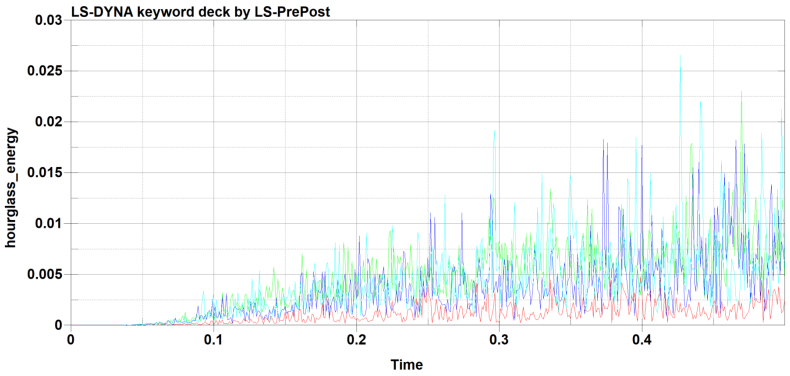

Figure B.2.5: Hourglass energy for low-energy parts.

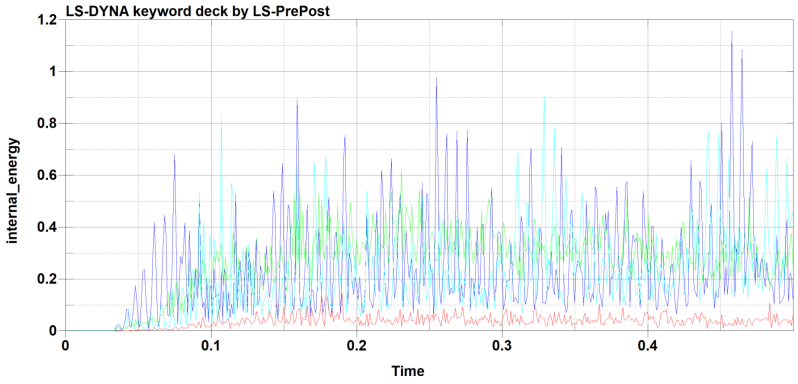

Figure B.2.6: Internal energy for low-energy parts.

B.3 Side collision

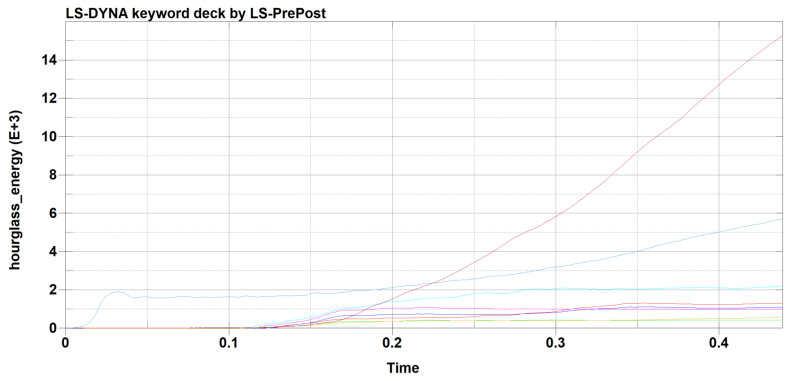

Figure B.3.1: Hourglass energy for high-energy parts.

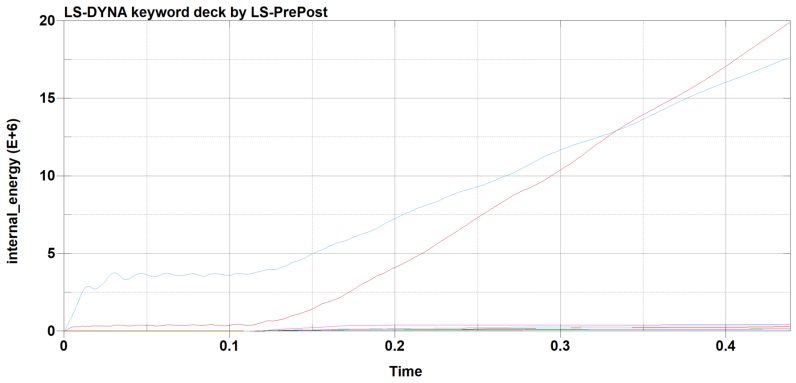

Figure B.3.2: Internal energy for high-energy parts.

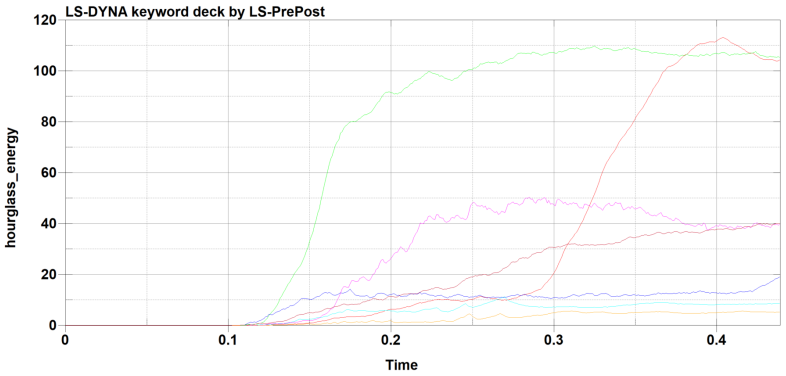

Figure B.3.3: Hourglass energy for medium-energy parts.

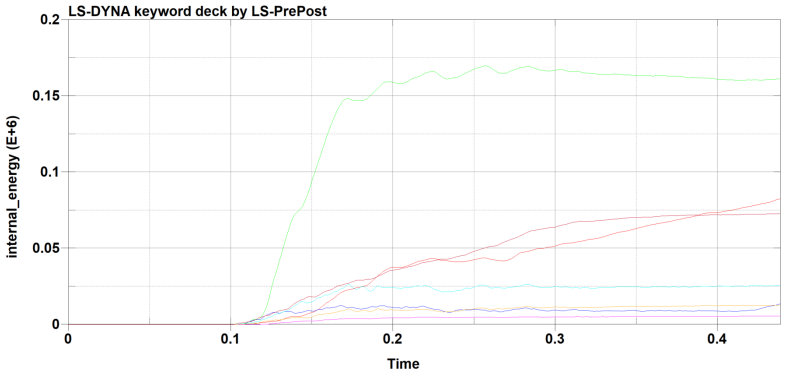

Figure B.3.4: Internal energy for medium-energy parts.

B.4 Stern corner collision

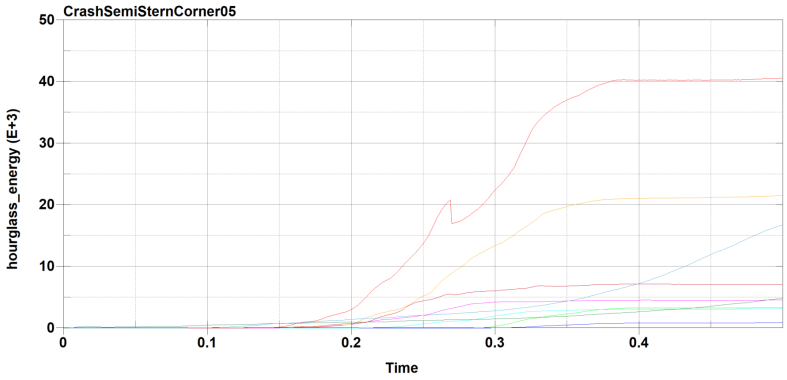

Figure B.4.1: Hourglass energy for high-energy parts.

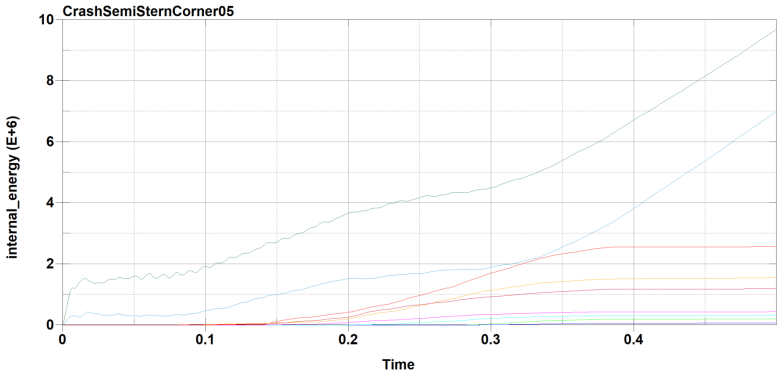

Figure B.4.2: Internal energy for high-energy parts.

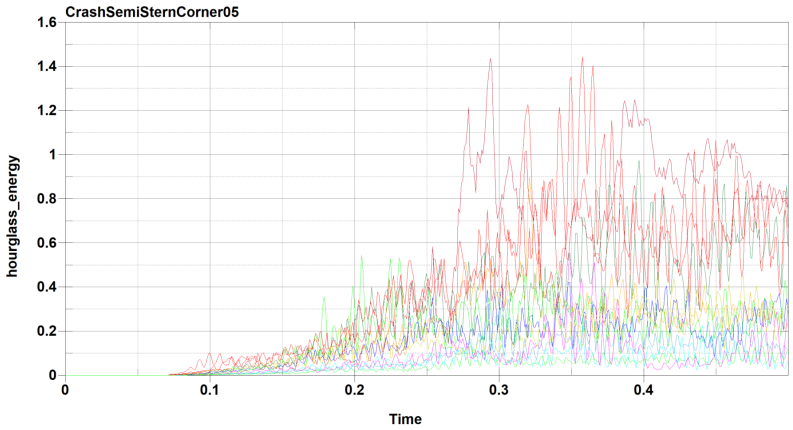

Figure B.4.3: Hourglass energy for medium-energy parts.

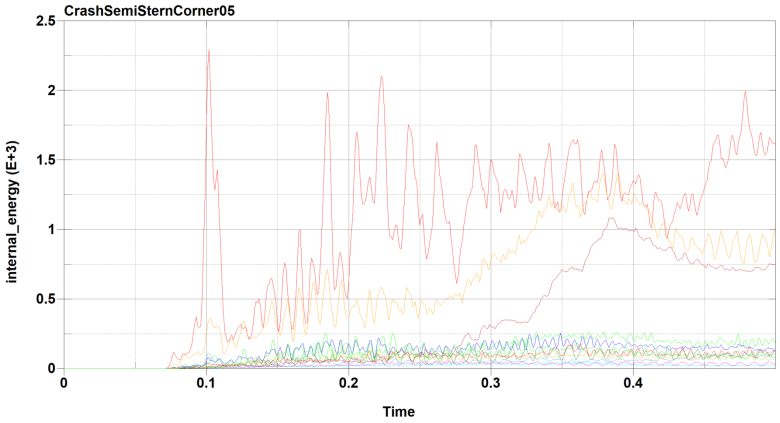

Figure B.4.4: Internal energy for medium-energy parts.

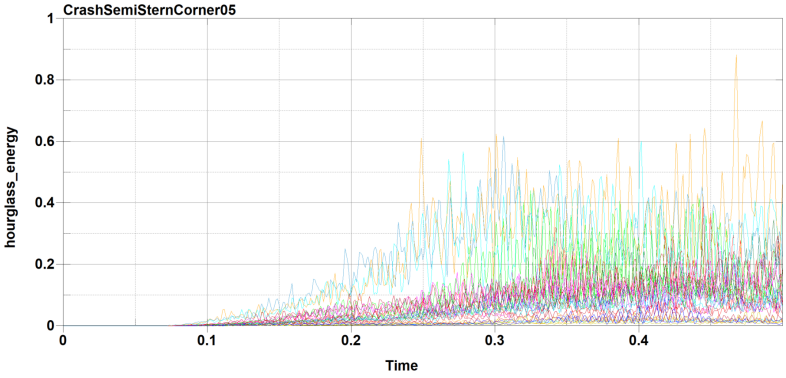

Figure B.4.5: Hourglass energy for low-energy parts.

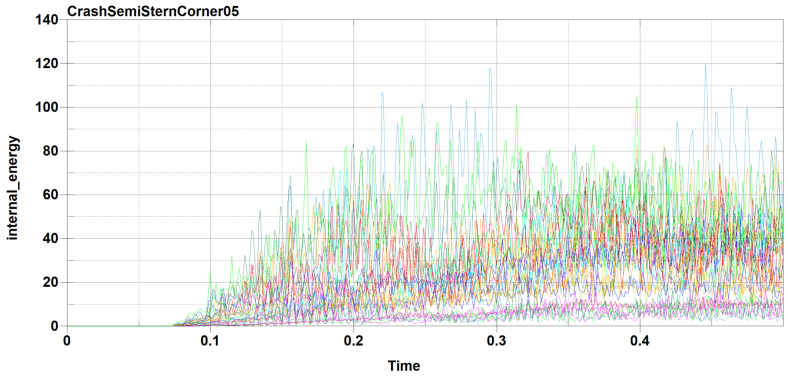

Figure B.4.6: Internal energy for low-energy parts.

C Vessel model specifications

C.1 bow model

Scantlings of structural components

Bulb second deck plate thickness	9 mm
Bulb bulkhead plate thickness	9 mm
Bulb longitudinal frame plate thickness	10.5 mm
Bulb transverse frame plate thickness	9.5 mm
Bulb breast hook plate thickness	12 or 15 mm
Bulb ring stiffeners	Flat Bar 250 mm × 15 mm, spacing 600 mm
Forecastle, 1st and 2nd deck, plate thickness	8 mm
Deck stiffeners	Flat Bar, web 160 mm (height) × 11.6 mm (thickness), length varies with location, spacing 0.6 m.
Deck girder	T type, web 385 mm × 10 mm, flange 150 mm × 9 mm, length varies with location, spacing 2.35 m
Stem hull plate thickness	Upper 9 mm, middle 11 mm, lower 12.8 mm
Bulb plate thickness	12.5 mm

Figure C.1.1: Information on bow model (Amdahl and Yu 2018).

C.2 Stern model

General dimensions

The stern 1 model and the bow model are from the same supply vessel.

Scantlings of structural components

Outer bottom plate thickness	11 mm
Inner bottom plate thickness	15 mm
Deck plate thickness	15 mm
Transverse frame	Thickness 10 mm, spacing 0.65 m
Longitudinal frame	Thickness 15 mm, spacing 0.65 m
Longitudinal stiffeners	L8.1 m × 0.32 m × 0.05 m × 12 mm, spacing 0.65 m
Side shell thickness	Lower 11 mm, upper 20 mm

Figure C.2.1: Information on stern model (Amdahl and Yu 2018).

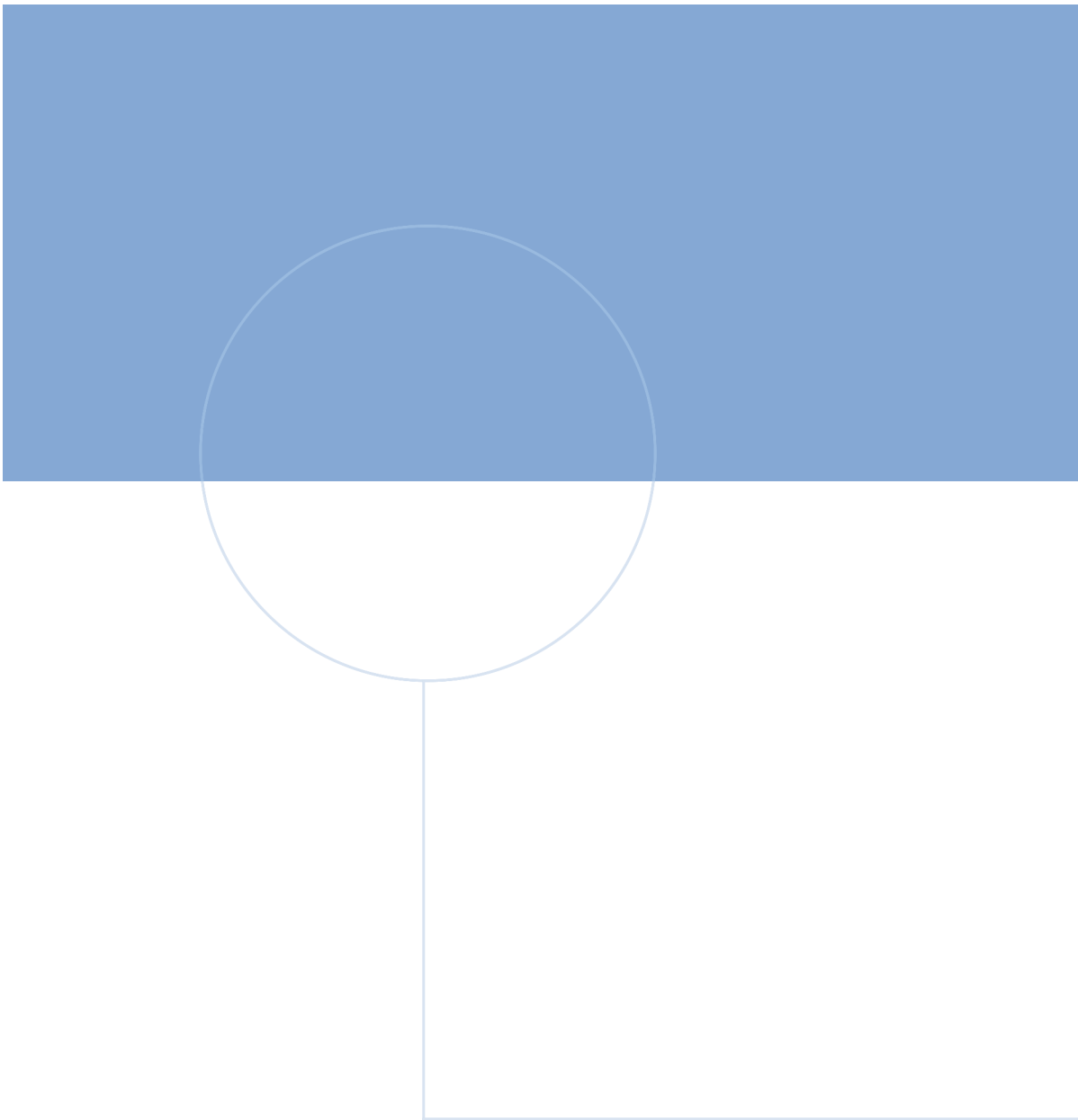

NTNU

Norwegian University of
Science and Technology